Mon. Not. R. Astron. Soc. **325**, 907–930 (2001)

Optical and infrared spectroscopy of the type IIn SN 1998S: days 3–127

A. Fassia,[1★] W. P. S. Meikle,[1] N. Chugai,[2] T. R. Geballe,[3] P. Lundqvist,[4] N. A. Walton,[5] D. Pollacco,[6] S. Veilleux,[7] G. S. Wright,[8] M. Pettini,[9] T. Kerr,[10] E. Puchnarewicz,[11] P. Puxley,[12] M. Irwin,[9] C. Packham,[13] S. J. Smartt[9] and D. Harmer[14]

[1]*Astrophysics Group, Blackett Laboratory, Imperial College, Prince Consort Road, London SW7 2BZ*
[2]*Institute of Astronomy, Russian Academy of Sciences, Ryatniskaya 48, 109017 Moscow, Russia*
[3]*Gemini Observatory Northern Operations Center, 670 N. A'ohoku Place, Hilo, Hawaii 96720, USA*
[4]*Stockholm Observatory, SE-133 36 Saltjöbaden, Sweden*
[5]*Isaac Newton Group, Apartado de Correos 321, 38780 Santa Cruz de La Palma, Islas Canarias, Spain*
[6]*Astrophysics and Planetary Sciences Division, The Queen's University of Belfast, Belfast BT7 1NN*
[7]*Department of Astronomy, University of Maryland, College Park, MD 20742-2421, USA*
[8]*Royal Observatory, Blackford Hill, Edinburgh EH9 3HJ*
[9]*Institute of Astronomy, Madingley Road, Cambridge CB3 0HA*
[10]*Joint Astronomy Centre, 660 N. A'Ohoku Place, University Park, Hilo, Hawaii 96720, USA*
[11]*Mullard Space Science Laboratory, University College London, Holmbury St. Mary, Dorking, Surrey RH5 6NT*
[12]*International Gemini Project, 950 N. Cherry Avenue, PO Box 26732, Tucson, AZ 85726-6732, USA*
[13]*Department of Astronomy, University of Florida, Gainesville, FL 32611, USA*
[14]*National Optical Astronomy Observatory, PO Box 26732, Tucson, AZ 85726, USA*

Accepted 2000 December 8. Received 2000 November 20; in original form 2000 October 4

ABSTRACT

We present contemporary optical and infrared spectroscopic observations of the type IIn SN 1998S covering the period between 3 and 127 days after discovery. During the first week the spectra are characterized by prominent broad H, He and C III/N III emission lines with narrow peaks, superimposed on a very blue continuum ($T \sim 24\,000$ K). In the following two weeks the C III/N III emission vanished, together with the broad emission components of the H and He lines. Broad, blueshifted absorption components appeared in the spectra. The temperature of the continuum also dropped to ~14 000 K. By the end of the first month the spectrum comprised broad, blueshifted absorptions in H, He, Si II, Fe II and Sc II. By day 44, broad emission components in H and He reappeared in the spectra. These persisted to as late as days ~100–130, becoming increasingly asymmetric. We agree with Leonard et al. that the broad emission lines indicate interaction between the ejecta and circumstellar material (CSM) emitted by the progenitor. We also agree that the progenitor of SN 1998S appears to have gone through at least two phases of mass-loss, giving rise to two CSM zones. Examination of the spectra indicates that the inner zone extended to ≤90 au, while the outer CSM extended from 185 au to over 1800 au.

We also present high-resolution spectra obtained at days 17 and 36. These spectra exhibit narrow P Cygni H I and He I lines superimposed on shallower, broader absorption components. Narrow lines of [N II], [O III], [Ne III] and [Fe III] are also seen. We attribute the narrow lines to recombination and heating following ionization of the outer CSM shell by the UV/X-ray flash at shock breakout. Using these lines, we show that the outer CSM had a velocity of 40–50 km s^{-1}. Assuming a constant velocity, we can infer that the outer CSM wind commenced more than 170 years ago, and ceased about 20 years ago, while the inner CSM wind may have commenced less than 9 years ago. During the era of the outer CSM wind the outflow from the progenitor was high – at least $\sim 2 \times 10^{-5}\,M_{\odot}\,yr^{-1}$. This corresponds to a mass-loss of at least $\sim 0.003\,M_{\odot}$, suggesting a massive progenitor. The shallower, broader absorption is of width ~350 km s^{-1}, and may have arisen from a component of the outer CSM shell produced when the progenitor was going through a later

★ E-mail: a.fassia@ic.ac.uk

blue supergiant phase. Alternatively, it may have been produced by the acceleration of the outer CSM by the radiation pressure of the UV precursor.

We also describe and model first-overtone emission in carbon monoxide observed in SN 1998S. We deduce a CO mass of $\sim 10^{-3}\,M_\odot$ moving at $\sim 2200\,km\,s^{-1}$, and infer a mixed metal/He core of about $4\,M_\odot$, again indicating a massive progenitor. Only three core-collapse supernovae have been observed in the *K* band at post-100 days, and all three have exhibited emission from CO.

Key words: circumstellar matter – supernovae: individual: SN 1998S.

1 INTRODUCTION

Core-collapse supernovae (SNe) are believed to arise from massive progenitors ($M \geq 8$–$10\,M_\odot$). The lower mass ($\sim$8–$10\,M_\odot$) and higher mass ($>20\,M_\odot$) progenitors experience heavy mass-loss during the final stages of their evolution, several solar masses being ejected via a range of mass-loss rates. Consequently, in the vicinity of some core-collapse supernovae, dense circumstellar material (CSM) would be distributed according to the mass-loss history of the progenitor. The subsequent interaction of the freely expanding supernova ejecta with the slowly moving CSM generates a fast shock wave in the CSM and a reverse shock wave in the ejecta. The shocked regions emit high-energy radiation. The intensity of this emission depends on the density of the CSM and the ejecta, and the shock acceleration of the ejecta during the explosion (Chevalier & Fransson 1994). If the density of the CSM is small, then the effects of the interaction only become significant several years after the explosion when the supernova has faded. However, if the CSM near the supernova is relatively dense, strong CSM–ejecta interaction can begin shortly after the explosion. This is the case for type IIn (n = narrow line) supernovae. These events exhibit narrow emission lines in their spectra superimposed on broader emission profiles. They also exhibit a strong blue continuum (Schlegel 1990). However, the broad P Cygni absorption components typical of normal type II SNe are weak or absent in type IIn SNe. The presence of variable, narrow-line emission is a direct manifestation of the excitation of the dense CSM by the SN radiation. In addition, the presence of broad Hα emission without a broad P Cygni absorption component is a clear indication that the observed broad-line emission is powered by the ejecta–wind interaction (Chugai 1990). Consequently, type IIn supernovae can provide unique information about the progenitor and its later evolution, through the observed properties of their CSM. In addition, the study of the interaction of these supernovae with the CSM can provide vital clues about galaxy evolution and the nature of active galactic nuclei (cf. Terlevich et al. 1992).

SN 1998S is the brightest type IIn event ever observed. It was discovered on 1998 March 2.68 UT in the highly inclined Sc galaxy NGC 3877 by Z. Wan (Li & Wan 1998) at a broad-band (unfiltered) optical magnitude of +15.2. The supernova is located at 16 arcsec west and 46 arcsec south of the nucleus. By March 18.4 it had brightened to $V = +12.2$ (Fassia et al. 2000). In a pre-discovery frame obtained on 1998 February 23.7 there was no evidence of the supernova, down to a limiting apparent magnitude of $\sim$+18 (Leonard et al. 2000; IAUC 6835). We can thus assume that SN 1998S was discovered within a few days of the shock breakout. In the present paper we have adopted the discovery date 1998 March 2.68 UT = JD 245 0875.2 as epoch 0 days, t_0, and express all other epochs relative to this fiducial date.

Optical spectra obtained about day 3 (March 5–6) by Filippenko & Moran (1998), Huchra (Garnavich et al. 1998) and ourselves (see day +3.3 spectrum in Fig. 1) showed prominent H and He emission lines with narrow peaks and broad wings, superimposed on a blue continuum. As mentioned above, these narrow lines indicate the presence of a dense CSM in the vicinity of the supernova. Using optical spectropolarimetry obtained at day 5, Leonard et al. (2000, hereafter L00) deduced that the CSM is asymmetrically distributed. Bowen et al. (2000) have presented high-resolution spectroscopy of interstellar and circumstellar lines towards SN 1998S. They suggest that the CSM comprises a dense shell expanding at $50\,km\,s^{-1}$, with a more highly ionized shell moving at $\sim 300\,km\,s^{-1}$. They also estimate that SN 1998S is at a real distance of $\sim$10 kpc from the nucleus, and deduce from the interstellar lines that it lies on the far side of the galaxy disc. Gerardy et al. (2000, hereafter G00) presented near-IR spectra of SN 1998S spanning 95–355 days post-maximum light. They identified emission from carbon monoxide. They also suggested that late-time multi-peak H and He line profiles in their optical and IR spectra indicate emission from a disc-shaped or ring-shaped circumstellar component. In addition, their $t \geq 225$ d, near-IR spectra exhibit a continuum that rises towards the longer wavelengths. They propose that the rising continuum is probably due to dust heated by the interaction of the ejecta with the CSM.

In Fassia et al. (2000) we presented contemporaneous optical and infrared photometric observations of SN 1998S covering the period between 11 and 146 days after discovery. Using the interstellar Na I D lines we derived an extinction $A_V = 0.68^{+0.34}_{-0.25}$ mag. We also examined the evolution of the total luminosity, and found that during the first month the luminosity decreased very rapidly, viz. $\sim 0.08\,mag\,d^{-1}$. Subsequently (days 30–70), the decline rate decreased, resembling that of type IIL supernovae viz. $0.05\,mag\,d^{-1}$. By day $\sim$100 the decline rate slowed to $0.01\,mag\,d^{-1}$ matching the radioactive decay of ^{56}Co. From the bolometric luminosity after $\sim$100 we estimate that $0.15 \pm 0.05\,M_\odot$ of ^{56}Ni were produced in the explosion. Furthermore, we discovered that as early as day 130 the supernova exhibited an astonishingly high IR excess, $K - L' = +2.5$. We argue that this excess is due to dust grains in the vicinity of the supernova. However, the physical extent of this early IR luminosity source was so large that the emission must have come from pre-existing dust in the CSM, possibly powered by X-rays from the CSM–ejecta interaction.

In this paper we present optical and infrared spectroscopy of SN 1998S covering the period 3–127 days after discovery. The observations and the reduction procedure are presented in Section 2. In Section 3 we discuss possible line identifications. In Section 4 we present an overview of the spectral behaviour of SN1998S, and derive constraints about the nature and the characteristics of the CSM. We also analyse and model the first overtone of the CO emission. The work is summarized in Section 5.

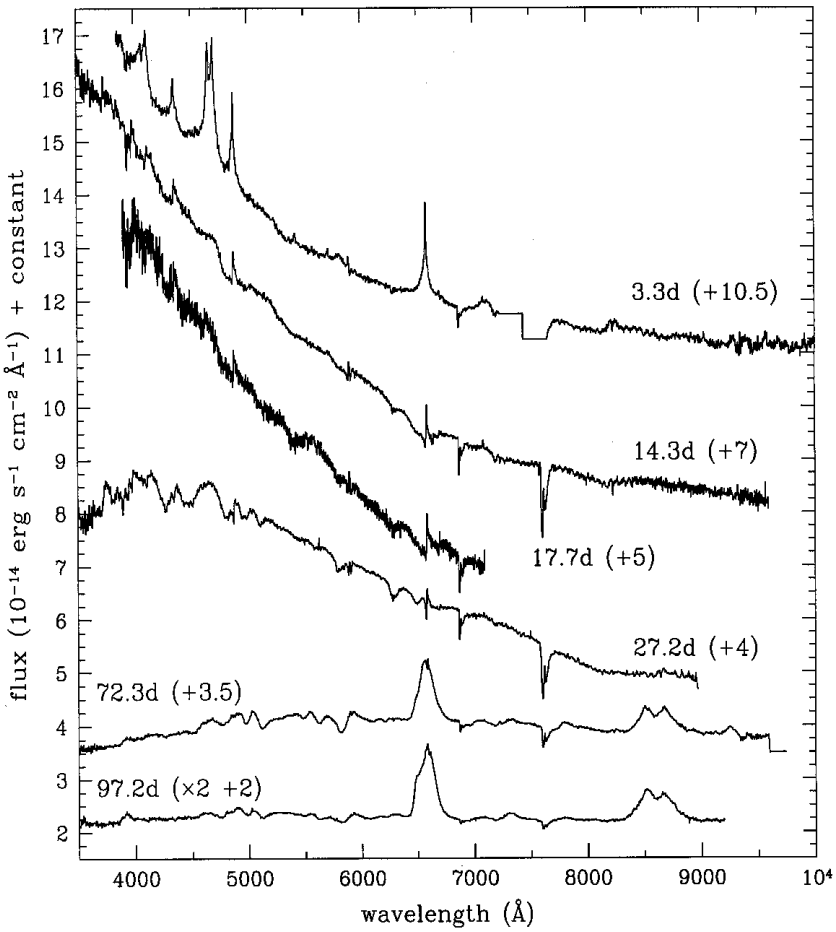

Figure 1. Optical spectra of SN 1998S taken at the Isaac Newton Telescope (La Palma) and the Wisconsin-Indiana-Yale-NOAO Telescope (Kitt Peak) (see Table 1 for details). The data have not been corrected for redshift or reddening. The epochs are with respect to the discovery date (1998 March 2.68 UT = 0 d). For clarity, the spectra have been displaced vertically by the amounts indicated (in units of 10^{-14} erg s^{-1} cm^{-2} Å^{-1}). The day 97.2 spectrum has also been multiplied by 2.

Table 1. Log of optical spectroscopy of SN1998S.

JD[a]	Date (1998 UT)	Epoch (d)	Telescope/ Instrument	Spectral Range λλ (Å)	Spectral Resolution Δλ (Å)	Slit Width (arcsec)	Spectrophotometric Standard[b]	Observer
878.5	March 6.0	3.3	INT/IDS	3850–10 337	6.75	1.46	SP1121+216	M. Irwin
889.5	March 16.8	14.3	INT/IDS	3390–9593	6.65	1.19	Feige 34	C. Packham & D. Pollacco
892.6	March 20.1	17.4	WHT/UES	4190–8856	0.12	2.00	–	J. Wood & S. Catalan
892.9	March 20.4	17.7	WIYN/Hydra	3904–7094	6.45	(3.1)[c]	GD140	D. Willmarth
902.4	March 29.9	27.2	INT/IDS	3393–8899	10.05	1.59	Feige 34	D. Pollacco
911.5	April 8.0	36.3	WHT/UES	3620–9424	0.14	2.36	–	S. J. Smartt
913.7	April 10.2	38.5	WIYN/Hydra	6425–6686	0.27	(3.1)[c]	α^2CVn	D. Harmer
947.5	May 14.0	72.3	INT/IDS	3485–9602	8.2	1.38	BD262606	D. Pollacco
972.4	June 7.9	97.2	INT/IDS	3398–9230	10.04	1.19	Feige 34	D. Pollacco

[a] 245 0000+
[b] Used to correct for atmospheric and instrumental transmission and to flux-calibrate the supernova spectra.
[c] This is a fibre-fed spectrograph. The diameter of the fibre used was 3.1 arcsec.

2 OBSERVATIONS

2.1 Optical spectroscopy

2.1.1 Low-resolution spectroscopy

Optical spectroscopy of SN 1998S was acquired using the ISIS spectrograph and the UES echelle spectrograph at the William Herschel Telescope (WHT), La Palma, the IDS spectrograph at the Isaac Newton Telescope (INT), La Palma, and the fibre-fed HYDRA spectrograph at the Wisconsin-Indiana-Yale-NOAO Telescope (WIYN), Kitt Peak. The log of optical observations is shown in Table 1.

Apart from the day 17.4 and day 36.3 UES spectra, the spectroscopic data were reduced by means of standard routines in the data-reduction package FIGARO (Shortridge 1995). The data were first cleaned of cosmic rays. Subsequently, the frames were

debiased, flat-fielded and sky-subtracted. The spectra were extracted from the resulting frames using simple extraction. Wavelength calibration was performed by means of Cu-Ar and Cu-Ne lamps. The spectrophotometric flux standards used are listed in Table 1.

Owing to adverse weather conditions and the use of fairly narrow slits (slit width $\leq$1.6 arcsec) in most cases, the fluxing described above was not accurate. Therefore, to improve the fluxing, we made use of our *BVR* photometry of SN 1998S (Fassia et al. 2000) to derive correction scaling factors. Transmission functions for the *B*, *V* and *R* bands were constructed using the JKT filter functions, the CCD response, and the standard La Palma atmospheric transmission. The spectra were then multiplied by these functions, and the resulting total flux within each band compared with the observed magnitudes. For dates where simultaneous photometric observations did not exist, we interpolated within the photometric data (Fassia et al. 2000). However, we do not have any photometry prior to day 11. Therefore, to scale the

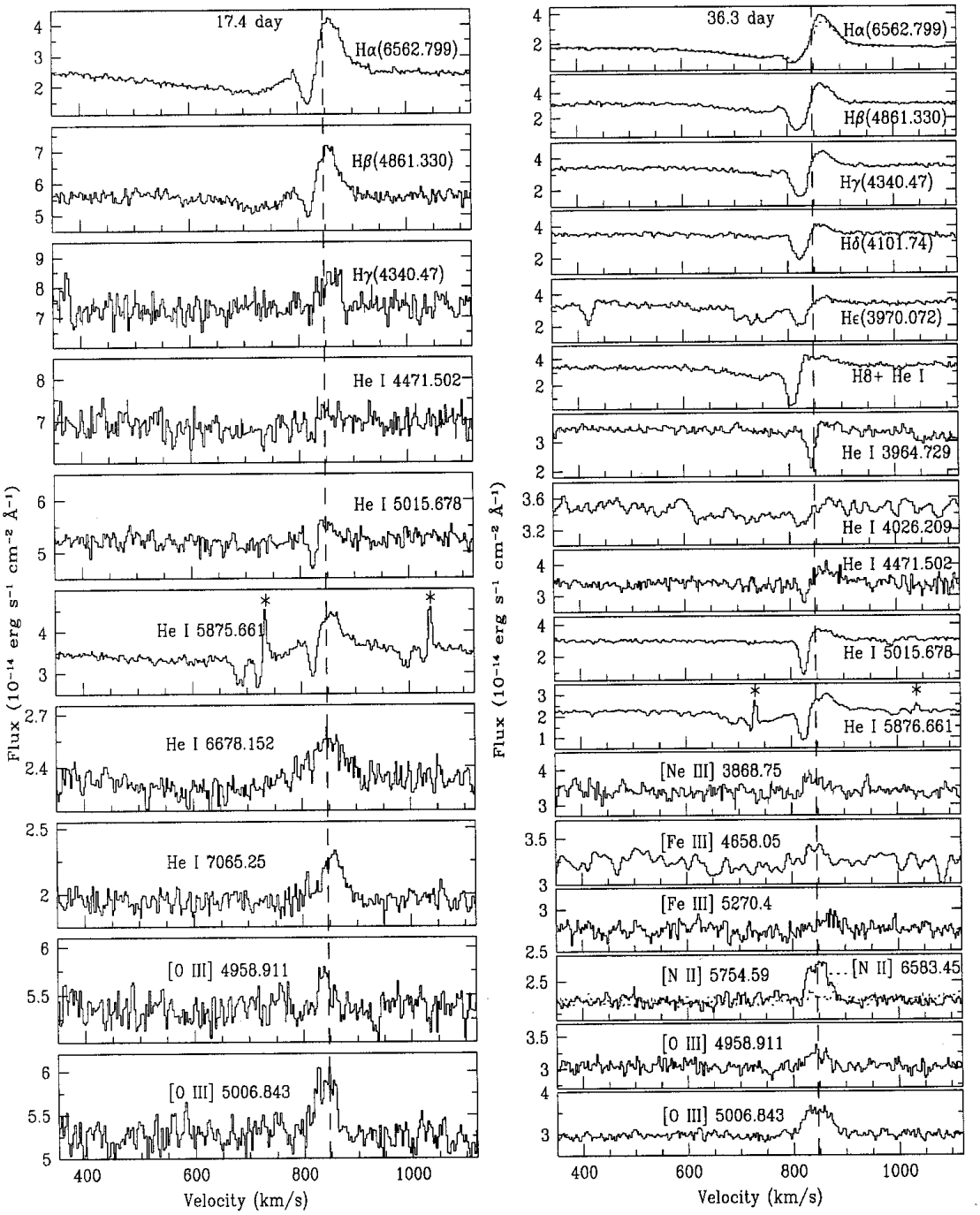

Figure 2. High-resolution (echelle) optical spectra of SN 1998S taken at the William Herschel Telescope (WHT) on days 17.4 and 36.3. Also shown as a dotted line on the top-right plot is the high-resolution spectrum of the H_α line obtained at the Wisconsin-Indiana-Yale-NOAO (WIYN) Telescope on day 38.5 (see Table 1 for details). The spectra have not been corrected for redshift. The Na I λ5889, 5895 night-sky lines are marked with an asterisk. The vertical dashed line corresponds to the adopted redshift for the SN centre of mass, 847 $\pm$ 3 km s^{-1} (cf. Section 3.2).

day 3.3 spectrum, we used *BVR* photometry (day 5) from Garnavich et al. (1999) together with *V*-band and unfiltered CCD photometry from the IAU circulars (IAUC 6829, IAUC 6831 and IAUC 6835) covering days 0–7.5 to interpolate to day 3.3. For any particular epoch the scaling factors derived for each band agreed to within ±10 per cent, demonstrating good internal consistency for the procedure. The spectra were multiplied by the geometric mean of the scaling factors for each epoch. The amounts by which the spectra had to be scaled to match the photometry ranged from ×1.23 to ×2.48. Including uncertainties in the photometry, we estimate the final absolute fluxing of the spectra to be accurate to ≤15 per cent. The optical spectra are shown in Fig. 1.

2.1.2 *High-resolution spectroscopy*

High-resolution optical spectra were obtained on days 17.4 and 36.3 with the WHT UES echelle spectrograph, and on day 38.5 with the WIYN Hydra spectrograph using a high-dispersion grating. Some of the UES spectra have already been presented and discussed in Bowen et al. (2000). The WHT/UES high-resolution spectra were reduced using the IRAF package ECHELLE. The data were bias-subtracted and flat-field-corrected. The different echelle orders were then traced and extracted from the frames. Wavelength calibration was by means of a thorium-argon lamp. We checked the precision of this calibration using night-sky emission lines present in our spectra, together with the high-resolution night-sky line atlas of Osterbrock et al. (1996). This demonstrated that our wavelength calibration is accurate to $\pm 2\,\mathrm{km\,s^{-1}}$.

Cosmic rays were present in the extracted spectra. These were identified and removed by comparing repeat observations of the spectra obtained at different times during the night. The counts in the contaminated pixels were then replaced by those of the corresponding pixels in the other spectrum. The mean fluxes of the spectra were then normalized to unity by fitting a low-order spline function to the instrumental continuum. Finally, the spectra were fluxed as follows. First, we determined the shape and flux of the overall SN continuum in the optical region at days 17.4 and 36.3. This was done by fitting a low-order spline function to the continuum in contemporary low-resolution spectra. This was straightforward for the earlier epoch, since a low-resolution spectrum was available on day 17.7. However, for day 36.3 no contemporary low-resolution spectrum was available. We therefore used the day 27.2 low-resolution spectrum scaled to match the *BVR* magnitudes on day 36.3. Given the evolution of the $B-V$ and $V-R$ colours, we can argue that the continuum shape did not change much during this period. We then scaled the normalized high-resolution spectra so that the continuum in the regions where lines were observed matched the continua determined from the low-resolution spectra. We estimate the fluxing of the high-resolution lines to be accurate to better than ±20 per cent. In Fig. 2 we show the spectral regions where lines are observed. Also shown in Fig. 2 is the high-resolution day 38.5 WIYN/HYDRA spectrum. The HYDRA spectra were reduced in the same way as the low-resolution optical spectra (cf. Section 2.1), and were fluxed following the same procedure as for the day 36.3 high-resolution spectra.

2.2 Infrared spectroscopy

Infrared spectra of SN 1998S were obtained at the United Kingdom Infrared Telescope (UKIRT), Hawaii, using the Cooled Grating Spectrograph CGS4. The observing log is shown in Table 2. During the observations the telescope was nodded 7.5 arcsec along the slit. The data were reduced using CGS4DR (Daly & Beard 1992) and FIGARO. After bias-subtraction and flat-field correction, the pair of images obtained at the two nod positions were subtracted to remove sky line emission. If residual sky line emission persisted, it was removed using POLYSKY. The positive and negative spectra were then extracted from the resulting frames, using the optimal extraction algorithm of Horne (1986). Wavelength calibration was by means of argon and krypton arc lamps. Observations of standard stars were used to correct for the atmospheric and instrumental transmission and to flux-calibrate the spectra. Hydrogen absorption lines in the standard star spectra were removed before these corrections/calibrations were performed. The standard stars used are listed in Table 2.

As with some of the optical spectra, variable weather

Table 2. Log of infrared spectroscopy of SN1998S obtained at UKIRT with CGS4.

JD[a]	Date (1998 UT)	Epoch (d)	Spectral Range λλ (Å)	Spectral Resolution Δλ (Å)	Slit Width (arcsec)	Spectrophotometric Standard[b]	Observer
878.0	March 5.5	2.8	18 870–25 200	66.5	2.46	HD84800	S. Veilleux
880.0	March 7.5	4.8	10 218–13 405	32.5	2.46	HD84800	S. Veilleux
882.0	March 9.5	6.8	9700–12 610	25.0	1.23	HD84800	E. Puchnarewicz
884.1	March 11.6	8.9	18 864–25 232	57.5	1.23	BS4761	P. Puxley
887.1	March 14.6	11.9	9926–13 099	25.1	2.46	BS4761	G. Wright
888.0	March 15.5	12.8	18 834–25 209	67.5	2.46	HD105601	G. Wright
892.9	March 20.4	17.7	10 215–13 402	20.5	1.23	BS4431	T. Geballe
919.8	April 16.3	44.6	9921–13 098	25.2	2.46	BS4550	T. Geballe
919.8	April 16.3	44.6	14 076–19 739	49.0	2.46	BS4550	T. Geballe
919.8	April 16.3	44.6	18 857–25 240	50.1	2.46	HD105601	T. Geballe
919.8	April 16.3	44.6	10 569–11 117	4.3	2.46	BS4550	T. Geballe
930.7	April 27.2	55.5	9770–12 971	18.9	1.23	BS4388	M. Pettini
930.8	April 27.3	55.6	10 579–11 129	3.3	1.23	BS4388	M. Pettini
983.8	June 19.3	108.6	18 747–25 071	49.3	2.46	BS4550	T. Kerr
988.8	June 24.3	113.6	10 087–13 285	16.9	1.23	BS4761	T. Geballe
1001.8	July 7.3	126.6	14 452–20 478	37.6	1.23	BS4572	T. Geballe

[a] 245 0000+
[b] Used to correct for atmospheric and instrumental transmission and to flux-calibrate the supernova spectra.

conditions, together with the use of narrow slits for some of the spectra, meant that fluxing using standard stars was approximate only. To improve the fluxing we could, in principle, follow a similar procedure to that applied to the optical spectra. However, no IR photometry was available until day 13.8, 11 days after our earliest IR spectrum. Moreover, for most of the *J*-band spectra the *J*-band photometry transmission function (filter + atmosphere + detector response) extended significantly beyond the red limit of the spectra.

For the earliest IR spectrum, which was at day 2.8 in *K*, there is a particular problem in checking the fluxing. Not only is there a lack of accurate photometry around this time, but also optical observations indicate that the light curve was rising rapidly, making it very difficult to make a flux correction using extrapolated magnitude values. However, the spectrum was taken in a wide (2.46-arcsec) slit, and so fluxing by means of the standard star is accurate to ± 20 per cent. Therefore no attempt was made to improve this fluxing.

For the other IR spectra we corrected the fluxing as follows. Using the optical and IR magnitudes given in Fassia et al. (2000), together with earlier optical magnitudes reported by Garnavich et al. (1999), we interpolated to provide magnitudes for each epoch upon which IR spectra were acquired. Thus a set of *UBVRI* magnitudes were established for epochs 4.8 to 8.9 d, and *UBVRIJHK* magnitudes for epoch 11.9 d onward. The magnitudes were then converted to fluxes using the calibrations of Wilson et al. (1972) and Bessel (1979). For epochs 4.8 to 8.9 d we fitted reddened blackbody functions to the *UBVRI* data. The blackbody functions were reddened using the empirical formula of Cardelli, Clayton & Mathis (1989), with $A_V = 0.68^{+0.34}_{-0.25}$ (Fassia et al. 2000). We then scaled the fluxes of the IR spectra so that the continua matched the blackbody functions (cf. Fig. 3). This procedure ignores the contribution of the optical emission lines to the blackbody fits, probably leading to an overestimate of the IR flux. However, from the day 3.3 optical spectrum, we estimate this systematic error was no more than 7 per cent. For epochs 11.9 to 17.7 d, while contemporaneous IR photometry was available, correction of the *J*-band spectra was still difficult due to the incomplete overlap problem explained above. Therefore, for the day 11.9 and 17.7 *J*-band spectra we followed a similar procedure to that carried out for the earlier epochs, except that now we included *JHK* photometry in the blackbody fits. Given the slow variation of the supernova flux around this time (cf. Fassia et al. 2000; Garnavich et al. 1999), we simply scaled the day 11.9 *J* spectrum so that its continuum matched the reddened blackbody day 14.3 optical spectrum. The day 12.8 18 834–25 240 Å spectrum was also flux-corrected by matching it to the same reddened blackbody. This spectrum was also checked using contemporaneous *H* and *K* light curves (see below). Similarly, the day 17.7 *J*-band spectrum was matched to the day 17.7 optical spectrum.

By epoch 44.6 d and later, the IR spectra were increasingly affected by emission/absorption features (cf. Figs 1, 4 and 5). Consequently, flux correction using the blackbody fitting procedure was increasingly inappropriate. Instead, for these later

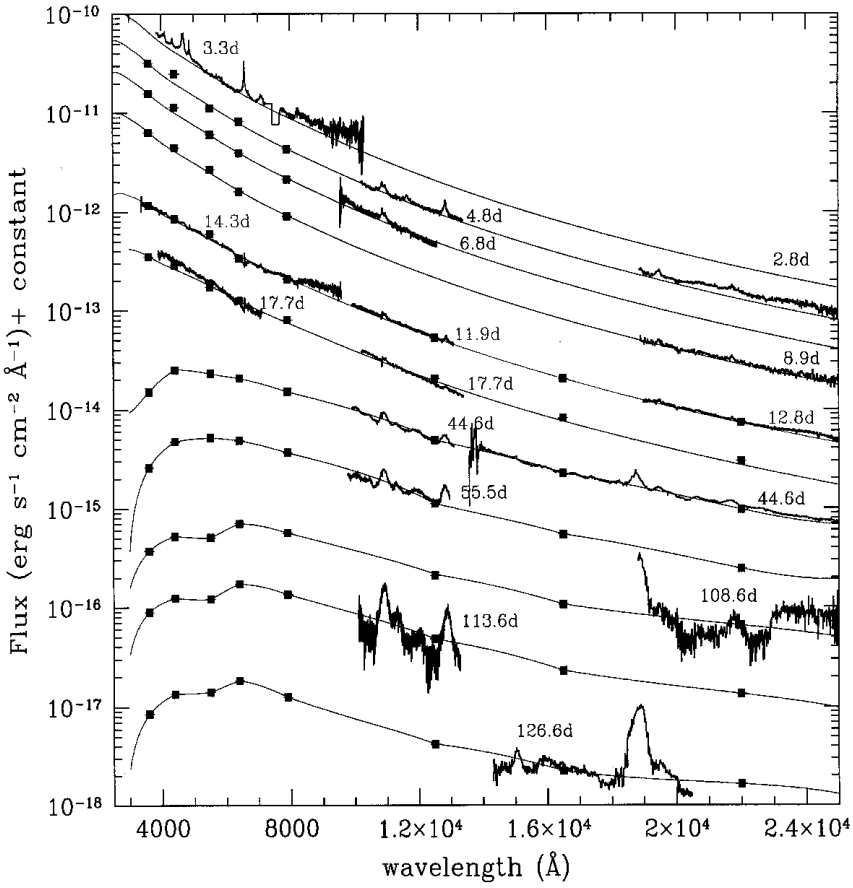

Figure 3. Blackbody fits ($t < 44.6$ d) and spline fits ($t \geq 44.6$ d) to *UBVRIJHK* photometry (see Section 2.2 for details). These fits were used to ascertain the absolute fluxing of the infrared spectra.

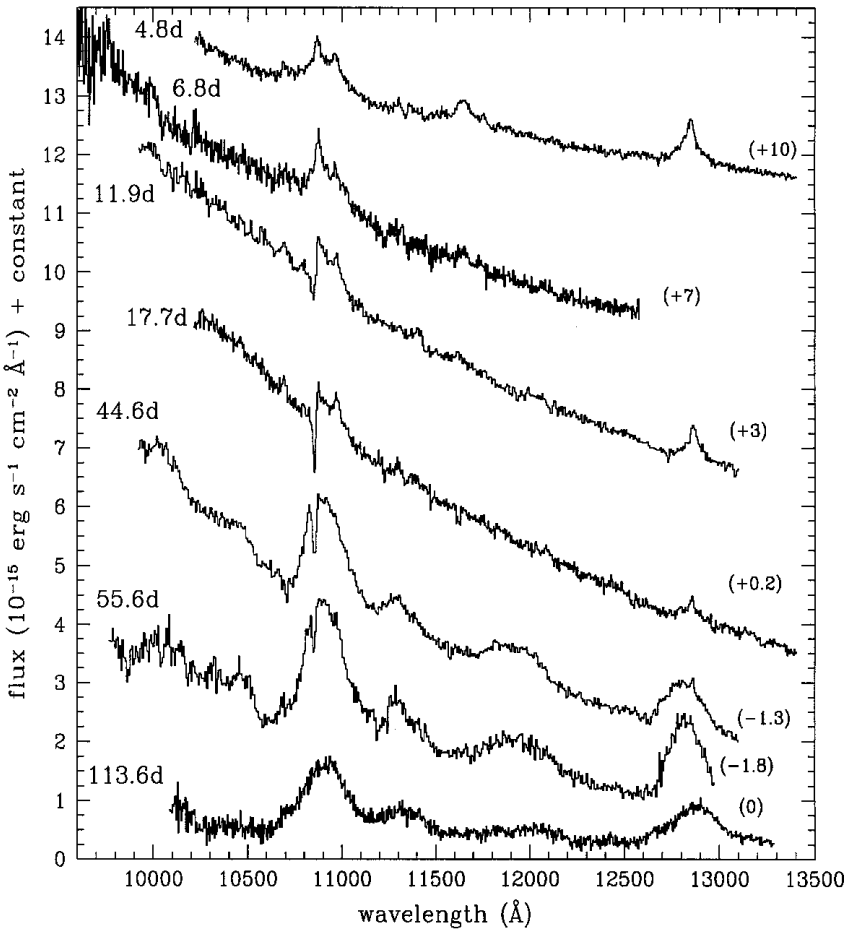

Figure 4. *J*-band spectra of SN 1998S taken at the United Kingdom Infrared Telescope (UKIRT). The spectra have not been corrected for redshift. The epochs are with respect to the discovery date (1998 March 2.68 UT = 0 d). For clarity, the spectra have been displaced vertically by the amounts indicated (in units of 10^{-15} erg s^{-1} cm^{-2} Å^{-1}).

epochs we applied spline fits (Press et al. 1992) to the *UBVRIJHK* photometry. We then scaled the IR spectra so that the integrated fluxes of the observed IR spectra and spline spectra were equal in the wavelength regions where they coincided (cf. Fig. 3). Scaling factors for the IR spectra ranged from ×0.92 to ×1.65.

To check the above scaling procedures, we used the optical flux correction method (Section 2.1) for the few IR cases where this was possible. Thus, using contemporary IR photometry (Fassia et al. 2000), we estimated absolute flux levels for the day 12.8 and 108.6 *K* spectra and the day 126.6 *H* spectrum. We constructed transmission functions for the *H* and *K* bands using the IRTF/UKIRT filter functions and the standard Mauna Kea atmospheric transmission. We then multiplied the corresponding spectra by these functions, and compared the resulting total fluxes with the photometry. The scaling factors derived by this procedure agreed to within 12 per cent with those derived by the blackbody/spline fits mentioned above. We estimate, therefore, that the absolute fluxing of the corrected IR spectra is accurate to $\lesssim$15 per cent. The final fluxed IR spectra are shown in Figs 4 and 5.

On days 44.6 and 55.6, high-resolution ($\sim$100 km s^{-1}) spectra of the He I 10 830-Å line were acquired with UKIRT/CGS4. They were wavelength-calibrated using sky lines from the raw images. Fluxing was carried out by scaling their continua to match the contemporary low-resolution spectra. They are shown in Fig. 6.

3 DESCRIPTION OF THE SPECTRA

3.1 Low-resolution spectra

In Figs 7 and 8 we redisplay the optical and IR spectra respectively, but with the best blackbody/spline fit continua (see Section 2.2) subtracted in order to minimize distortion of the line profiles. In addition, the relative flux is plotted logarithmically in order to bring out the detail in the line profiles. The spectra have not been redshift-corrected. The resulting line identifications are indicated in Tables 3 and 4, and in Figs 7 and 8. In general, the lines have complex profiles comprising mixtures of broad and narrow emission and absorption lines. To examine these profiles in detail, we carried out multiple component fits using Gaussian profiles. This provided peak wavelengths, intensities and widths of the separate components of each profile. These are listed in Tables 3 and 4 for the optical and IR spectra respectively. We note that the presentations of L00 and G00 include first-season optical and IR spectra which have similar epochs to some of the spectra discussed here.

3.1.1 Days 3–7

During the first week, the spectra are characterised by strong, complex emission lines of the Balmer, Paschen and Brackett

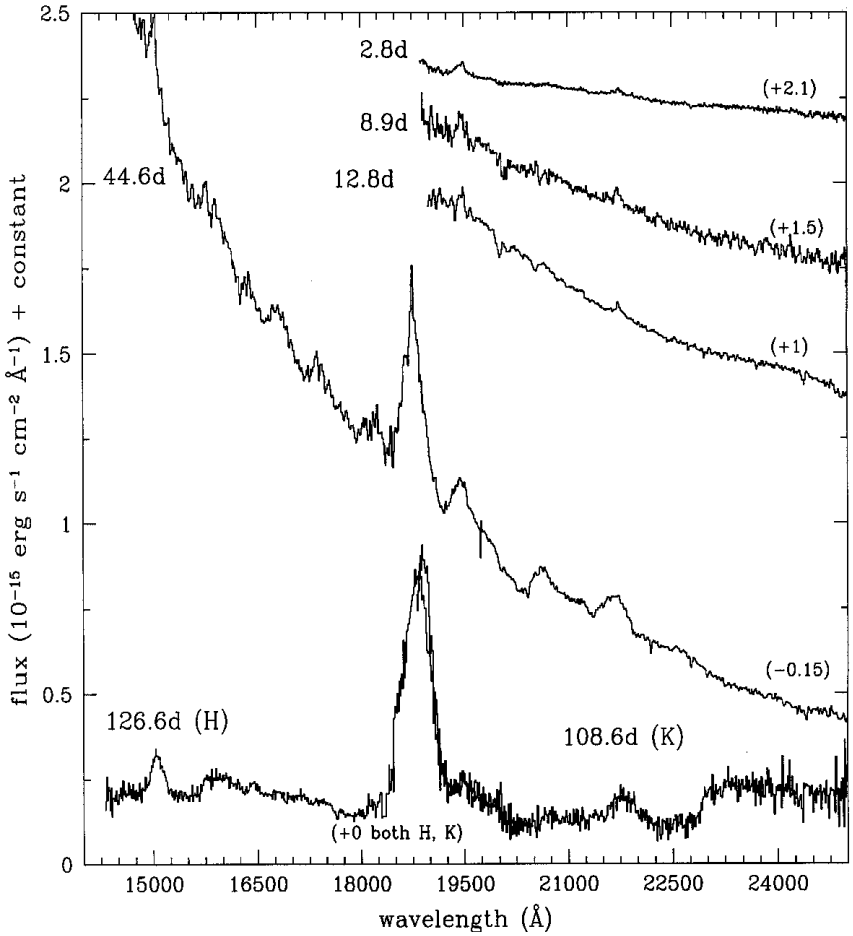

Figure 5. *H*- and *K*-band spectra of SN 1998S taken at the United Kingdom Infrared Telescope (UKIRT). The spectra have not been corrected for redshift. The epochs are with respect to the discovery date (1998 March 2.68 UT = 0 d). For clarity, the spectra have been displaced vertically by the amounts indicated (in units of 10^{-15} erg s^{-1} cm^{-2} Å^{-1}).

series, He I 10 830 Å, He II 4686 Å and C III 4648/N III 4640 Å, lying on a smooth blue continuum. There is little sign of any absorption components. In Fig. 3 we show blackbody spectra reddened by $E(B-V) = 0.22$ ($R_V = 3.1$) superimposed on the optical and IR continua. The blackbody temperature on day 3.3 is 23 600 ± 500 K. A somewhat higher blackbody temperature of 28 000 K is derived by L00 for their day 4 optical spectrum, using a slightly higher $E(B-V)$ of 0.23. They point out that this is quite high for a type II SN at this epoch. In agreement with L00, we also find that the day 3–4 blackbody fit fails to account for all the continuum blueward of ~5000 Å. L00 argue that the most likely cause is a departure from the blackbody spectrum due to the increase of the continuum absorptive opacity (bound–free, free–free) with wavelength. We confirm the L00 finding that a typical line profile at this time comprises a narrow unresolved component superimposed on a broad base (cf. Figs 7 and 8). This is illustrated in Figs 9 and 10, where we show multiple Gaussian component fits to Hα and He I 10 830 Å respectively. The unresolved component has a FWHM $\leq 500\,\mathrm{km\,s^{-1}}$, superimposed on a broad component of FWHM ~4000 km s^{-1}. Other broad emission features include one at ~7100 Å, which we attribute to a blend of He I 7065 Å and C II 7100 Å. Other narrow lines include C III 5696 Å, He I 5876, 6678, 7065 Å and He II 5411, 8236 Å (possibly) and 11 626 Å. Note that the narrow absorption feature at 20 000 Å is residual absorption due to H_2O, CO_2 and CH_4 vapour in the Earth's atmosphere.

3.1.2 *Days* 8–18

Between days 3.3 and 17.7, blackbody fits indicate a cooling continuum. By day 17.7 the blackbody temperature was 14 500 K, consistent with the 13 400 ± 1200 K derived by Fassia et al. (2000) from contemporary photometry. During this time, the lines also underwent a substantial change. Between days 3.3 and 14.3 the broad emission component in Balmer, Paschen, Brackett and He I 10 830 Å lines largely vanished (see also Qiu et al. 1998), leaving behind narrower, but still quite complex, emission features. The intense C III 4648/N III 4640 Å feature disappeared altogether. The disappearance of the broad emission in the Balmer and He I 10 830-Å lines was accompanied by the appearance of a broad, blueshifted absorption extending to velocities of ~10 000 km s^{-1}. However, broad absorptions did not appear in the Paschen or Brackett lines. In Hα and He I 10 830 Å, weak, unresolved (FWHM $\leq 500\,\mathrm{km\,s^{-1}}$) P Cygni profiles developed. These narrow lines are examined in greater detail in Section 3.2.

3.1.3 *Days* 27–56

The day 27 optical spectrum is very similar in appearance to the day 25 spectrum of L00. In making line identifications, we were guided by those given for the photospheric spectra of the type II SN 1987A and SN 1995V (Williams 1987; Fassia et al. 1998). By

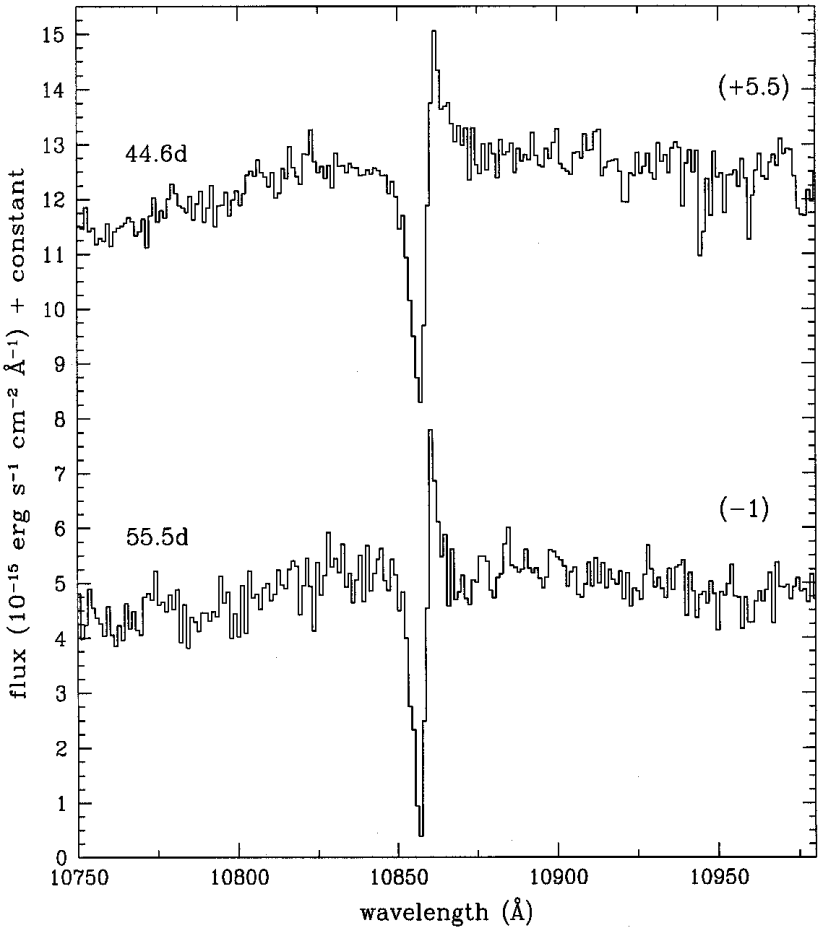

Figure 6. High-resolution spectra of SN 1998S taken at the United Kingdom Infrared Telescope (Hawaii). The epochs are with respect to the discovery date (1998 March 2.68 UT = 0 d). For clarity, the spectra have been displaced vertically by the amounts indicated (in units of 10^{-15} erg s^{-1} cm^{-2} Å^{-1}).

day 27 the spectrum comprises broad, blueshifted absorptions in H (Balmer series), He I + Na I blend, Si II, Fe II and Sc II, together with narrow P Cygni lines of H (Balmer series), He I and narrow emission lines of [O III]. (Narrow emission lines of [N II], [Ne III] and [Fe III] were also seen around this time in our high-resolution spectra – see Section 3.2). The FWHM of the broad absorptions is $\sim$4000 km s^{-1}, with the minima blueshifted by 4000–5500 km s^{-1} with respect to the local standard of rest. The blue edge of the Hα absorption trough is blueshifted by $\sim$8000 km s^{-1}. In the IR spectra, by days 44 and 55, broad emission features (FWHM $\sim$5000 km s^{-1}) had developed in the Paschen, Brackett and He I 10 830-Å lines. The FWHM of the Paα, Paβ and Brγ lines on day 44.6 is $\sim$5000 km s^{-1}. A broad, blueshifted absorption in He I 10 830 Å is also apparent. The deep narrow absorption seen in He I 10 830 Å on day 17 is still present on days 44 and 55. This is discussed in Section 3.2. Other broad IR features that had appeared by this period we identify with blends of O I 11 287/94–S I 11 306 Å, and Mg I 11 828–Si II 12 047 Å (cf. Meikle et al. 1989). L00 note that the relative strengths of some of the broad features in the optical spectrum resemble those found in the spectra of SNe Ic, suggesting hydrogen-deficient ejecta. They also suggest that the low contrast of the broad lines relative to the continuum may be due to external illumination of the line-forming region by light from the CSM–ejecta interaction (see also Branch et al. 2000 and Lentz et al. 2001). This is discussed in more detail in Section 4.1.2.

3.1.4 Days 72–127

Between days 27 and 72 in the optical region the most striking change is the replacement of the fairly weak, broad P Cygni Hα feature with a strong, broad (FWHM $\sim$ 7000 km s^{-1}) emission feature (cf. Fig. 7). The profile is somewhat asymmetric. Its peak is blueshifted by ~ -500 km s^{-1} with respect to the SN rest frame, and its blue wing is steeper. The extreme limit of the blue wing is blueshifted by ~ -8500 km s^{-1}. The observation of comparably wide Paschen emission lines on day 44.6 suggests that broad Hα emission had probably already appeared by then. In other Balmer lines, the change from days 27 to 72 was less dramatic. The absolute depth of the broad absorption in Hβ weakened, and the Hγ absorption disappeared almost entirely by day 97. A dramatic change between days 27 and 72 is the appearance of strong, broad emission in the Ca II IR triplet. The presence of O I 7773-Å and O I 9264-Å emission lines on the day 72 spectrum suggests that significant emission from the O I 8446-Å line may be blended with the Ca II multiplet. The broad absorption lines in the He I + Na I blend, Fe II and Sc II became more pronounced, but vanished in Si II 6355 Å. The narrow H I and He I lines had weakened by day 72, with only Hα being clearly visible. Weak narrow [O III]4959, 5007 Å lines are visible in the day 97 spectrum.

Our day 97 optical spectrum is similar to the day 108 spectrum of L00, and our day 109/113/127 composite IR spectrum is similar to the day 110 spectrum described in G00. By this period, the

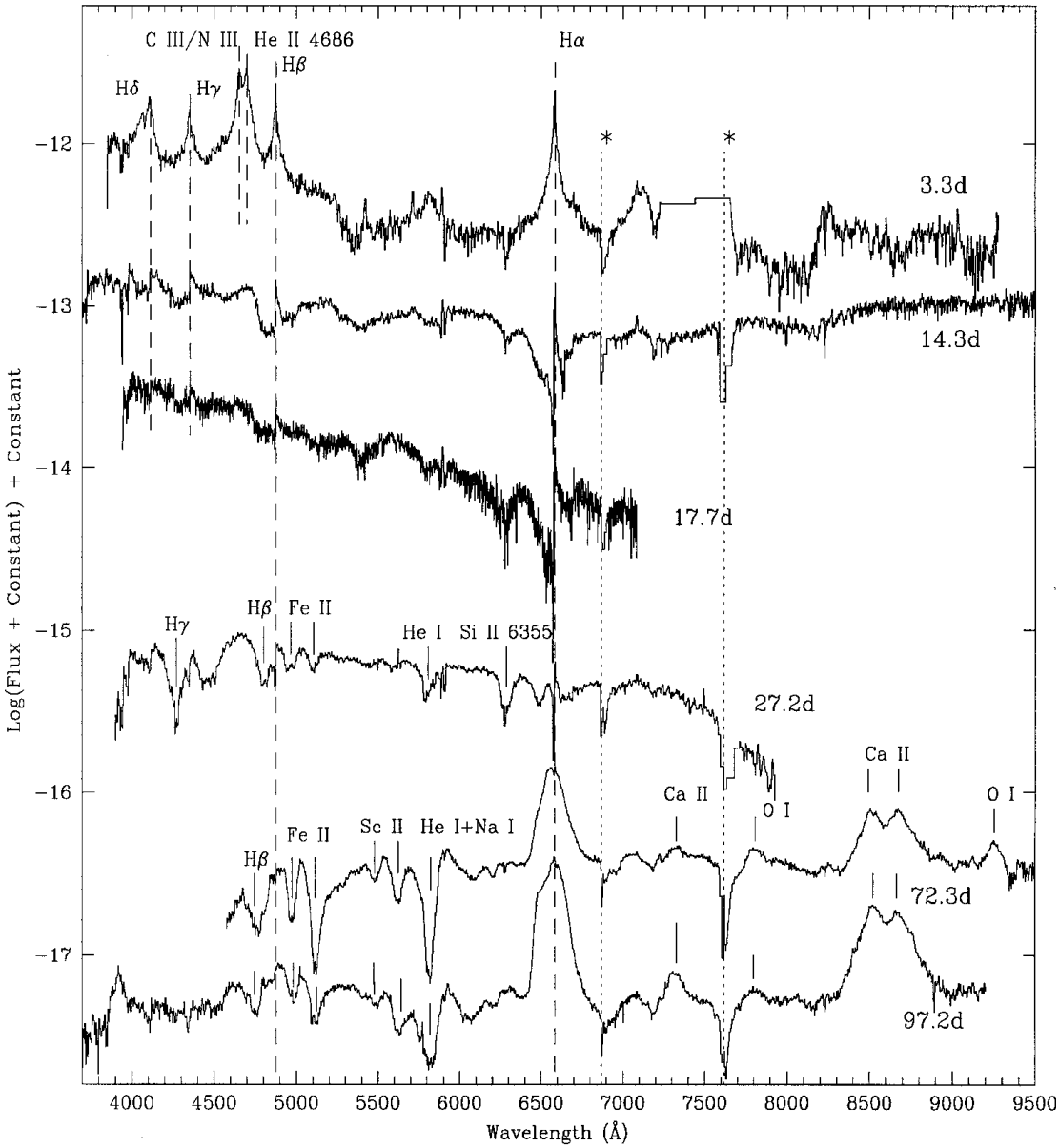

Figure 7. Optical spectra of SN 1998S with blackbody/spline fit continua shown in Fig. 3 subtracted. Suggested line identifications are indicated. (The dashed lines correspond to the rest wavelength of the lines in NGC 3877.) Residual telluric absorption lines are marked with the dotted lines and an asterisk.

spectra were dominated by broad emission lines of Hα, Paα, Paβ, Paγ + He I 10 830-Å blend and the Ca II triplet. The Hα, Paα and Paβ lines had broadened to a FWHM of 7000–8500 km s^{-1}. Moreover, the Hα, and possibly Paα, profiles had become more asymmetric, with the development of a pronounced steep blue edge. The asymmetry, and the pronounced red wings of these lines could indicate that Thomson scattering of line radiation occurred in the ejecta during this epoch. We note, however, that Brγ had weakened significantly. Also of importance is the appearance by day 109 of first-overtone emission from carbon monoxide. This is discussed further in Section 4.2. L00 suggest that the appearance of broad, asymmetric Hα emission in their day 108 spectrum is due to interaction of the ejecta with that part of the CSM responsible for the narrow lines seen at earlier epochs. We support this proposal, and suggest that the presence of strong, broad Paschen and Brackett lines on day 44 indicates that the interaction may have already begun as early as this. This will be discussed further in Section 4.

3.2 High-resolution spectra

The WHT/UES observations of SN 1998S on days 17.4 and 36.3 revealed narrow absorption and emission lines. Many of the absorption lines have widths of around 2–15 km s^{-1}, and can be attributed to the interstellar medium (ISM) of the Milky Way and NGC 3877. Fassia et al. (2000) used the Na I D absorption lines observed on day 36.3 to estimate the extinction to SN 1998S. In a more comprehensive analysis of the WHT/UES ISM data, Bowen et al. (2000) examined a range of lines in the UV and optical regions. They also describe a blueshifted absorption feature in Mg II 2796 Å and in the Balmer lines, of width $\sim$350 km s^{-1}. Variation in the depth of these features between different epochs

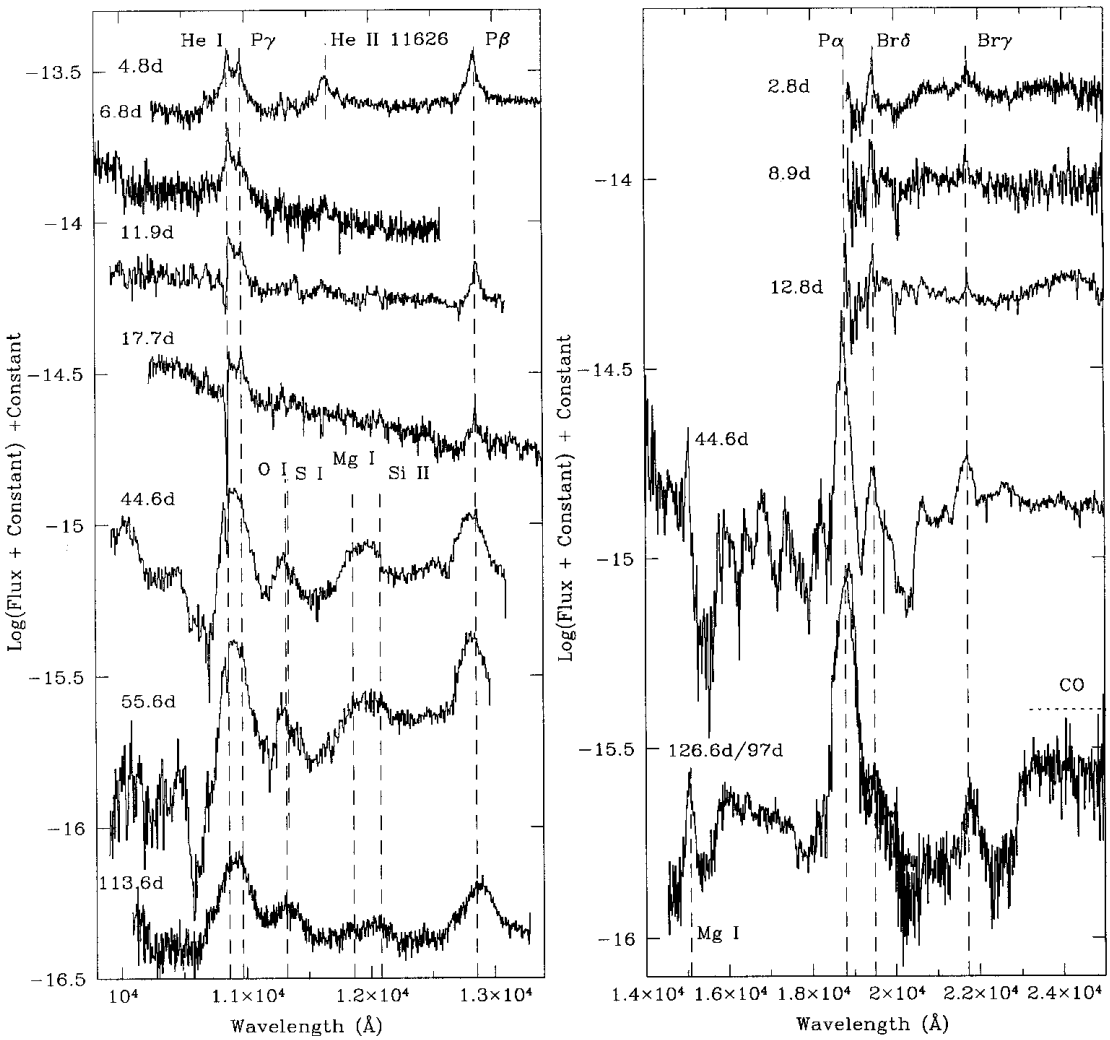

Figure 8. Infrared spectra of SN 1998S with the blackbody/spline fit continua shown in Fig. 3 subtracted. Suggested line identifications are indicated. (The dashed lines correspond to the rest wavelength of the lines in NGC 3877.)

points to an origin in the CSM. A variable, narrow component in Na I D is also attributed to the CSM. In addition, Bowen et al. report the presence of narrower ($\sim$30 km s^{-1}) Balmer and optical He I P Cygni lines, as well as similarly narrow P Cygni lines in a number of Fe II UV multiplets. These too are attributed to the CSM of SN 1998S. They also indicate (in their table 4) the presence on day 36.3 of narrow forbidden lines of [N II], [Ne III], [O III] and [Fe III], and suggest an origin in either the CSM or some other line-of-sight emission-line region.

In the present work we consider only those narrow lines whose origin is in the CSM of SN 1998S. In Fig. 2 we display and identify all the CSM lines present in the day 17.4 and day 36.3 WHT/UES spectra (resolution $\sim$7 km s^{-1}). Also shown is the day 38 Hα profile (resolution $\sim$12 km s^{-1}) obtained at the WIYN. In Fig. 6 we show the high-resolution ($\sim$100 km s^{-1}) P Cygni spectra of the He I 10 830-Å line acquired with UKIRT/CGS4 on days 44.6 and 55.6. In the optical spectra we confirm the presence of most of the allowed and forbidden lines described in Bowen et al. (2000). In particular, we confirm that the H lines are composed of two components, viz. a narrow P Cygni-like profile superimposed on a broader absorption feature which extends as far as ~ -350 km s^{-1} to the blue. We also note the presence of a similar broad absorption in He I 5876 Å and possibly, in He I 4471, 5016 Å. Identifications of the narrow lines are listed in Table 5, along with the redshifts of the emission peaks, the blueshifts of the P Cygni troughs relative to the estimated SN centre of mass (see below), the widths of the emission and absorption components and the line intensities. The narrow H profiles span a range of $\sim$130 km s^{-1}, the He I profiles span $\sim$100 km s^{-1}, while those of the forbidden lines span $\sim$80 km s^{-1}.

Two of the narrow emission lines which Bowen et al. (2000) list in their table 4, they identify as He I 3870 Å and O I 7773 Å. We confirm the presence of these features. However, it seems unlikely that they originate in the SN CSM. First, both lines are unresolved, implying a linewidth of less than $\sim$10 km s^{-1}. This is much narrower than the FWHM $\sim$ 60 km s^{-1} which is typical of the emission components of other narrow lines. The 'He I 3870-Å' feature can be seen in Fig. 2 lying $\sim$100 km s^{-1} redward of [Ne III] 3869 Å. In the case of this line, comparison of two successive repeat frames shows that it appeared strongly only in the first, while in the second it was not discernible above the noise. In the case of the 'O I 7773-Å' line, we note that it extends the full length of the slit (15 arcsec), equivalent to over 1 kpc at NGC 3877. It is also at the wrong redshift for it to be associated

Table 3. Line identification in the optical spectra of SN1998S.

		March 5.8 3.3d			March 16.9 14.3d			March 20.4 17.7d			March 29.9 27.2d			May 14.0 72.3d			June 7.9 97.2d		
ID	LS[a]	λ_{peak}(Å)	FWHM(Å)	FLUX[b]	λ_{peak}(Å)	FWHM(Å)	FLUX[b]	λ_{peak}(Å)	FWHM(Å)	FLUX[b]	λ_{peak}(Å)	FWHM(Å)	FLUX[b]	λ_{peak}(Å)	FWHM(Å)	FLUX[b]	λ_{peak}(Å)	FWHM(Å)	FLUX[b]
He	BE	-	-	-	4001.2(2.6)	28.2(4.1)	0.80(0.25)	-	-	-	-	-	-	-	-	-	-	-	-
	NE	-	-	-	3985.3(0.3)	4.4(0.7)	0.15(0.03)	-	-	-	-	-	-	-	-	-	-	-	-
	NA	-	-	-	3978.1(0.3)	4.5(0.3)	0.22(0.02)	-	-	-	-	-	-	-	-	-	-	-	-
Sr II 4077	NA	-	-	-	-	-	-	-	-	-	4074.8(1.4)	8.8(1.9)	0.12(0.04)	-	-	-	-	-	-
Hδ	BE	4108.7(5.1)	84.1(7.3)	4.02(1.10)	4141.8(3.3)	44.1(8.6)	0.75(0.35)	-	-	-	-	-	-	-	-	-	-	-	-
	BA	-	-	-	-	-	-	-	-	-	4072.0(7.9)	93.3(9.4)	1.75(0.35)	-	-	-	-	-	-
	NE	4108.8(2.0)	24.1(4.5)	1.16(0.37)	4115.6(0.4)	8.6(0.7)	0.27(0.02)	-	-	-	-	-	-	-	-	-	-	-	-
	NA	-	-	-	4097.0(0.4)	8.7(1.5)	0.20(0.05)	-	-	-	4107.2(2.1)	13.3(3.9)	0.25(0.11)	-	-	-	-	-	-
Hγ	BE	4353.8(4.9)	69.9(13.7)	2.68(0.57)	4370.3(4.7)	45.6(9.7)	1.17(0.35)	4365.9(2.8)	32.7(11.2)	1.54(0.35)	-	-	-	-	-	-	-	-	-
	NE	4349.5(2.0)	12.0(4.9)	0.6(0.2)	4354.3(0.3)	6.9(0.5)	0.25(0.03)	-	-	-	-	-	-	-	-	-	-	-	-
	BA	-	-	-	-	-	-	-	-	-	4271.4(5.2)	103.0(14.5)	5.96(1.9)	-	-	-	-	-	-
	NA	-	-	-	4343.3(2.0)	19.2(2.9)	0.29(0.07)	-	-	-	4344.3(1.5)	16.8(3.2)	0.38(0.14)	-	-	-	-	-	-
He I 4471	BA	-	-	-	-	-	-	-	-	-	4468.6(11.2)	130.2(26.0)	8.0(1.7)	-	-	-	-	-	-
He II 4686	BE[c]	4677.8(2.6)	101.7(5.6)	15.2(1.06)	-	-	-	-	-	-	-	-	-	-	-	-	-	-	-
	NE	4696.3(1.2)	14.0(1.2)	1.25(0.16)	-	-	-	-	-	-	-	-	-	-	-	-	-	-	-
C III 4648/N III 4640	NE	4650.9(0.6)	15.9(0.5)	1.4(0.08)	-	-	-	-	-	-	-	-	-	-	-	-	-	-	-
Hβ	BE	4873.0(2.2)	62.6(7.5)	3.98(0.34)	4888.5(1.7)	26.4(1.8)	0.65(0.09)	4893.7(10.4)	33.2(8.2)	0.67(0.10)	-	-	-	-	-	-	-	-	-
	NE	4873.4(0.5)	9.2(0.9)	1.02(0.11)	4875.6(0.2)	9.4(0.4)	0.44(0.03)	4876.6(1.7)	10.6(4.9)	0.35(0.18)	4882.8(4.7)	17.8(4.9)	0.30(0.16)	-	-	-	-	-	-
	BA	-	-	-	-	-	-	-	-	-	4802.7(11.2)	95.7(18.1)	4.23(1.9)	4765.8(6.1)	122.2(15.6)	2.05(0.25)	4753.9(4.5)	64.5(15.5)	0.31(0.08)
	NA	-	-	-	4867.1(0.7)	9.2(1.1)	0.17(0.04)	4869.6(1.2)	6.0(1.2)	0.22(0.07)	4870.4(1.7)	9.9(0.9)	0.39(0.08)	-	-	-	-	-	-
Fe II 5018	BA	-	-	-	-	-	-	-	-	-	4965.6(11.2)	96.3(14.6)	3.06(0.7)	4974.4(1.1)	56.6(14.5)	1.38(0.15)	4982.4(2.6)	45.8(10.2)	0.21(0.09)
Fe II 5169	BA	-	-	-	-	-	-	-	-	-	5106.1(6.0)	70.1(10.7)	1.60(0.32)	5118.1(1.3)	80.8(3.2)	2.17(0.5)	5123.9(4.6)	86.9(11.5)	0.56(0.18)
He II 5411	NE	5419.7(1.2)	23.7(4.0)	0.38(0.07)	-	-	-	-	-	-	-	-	-	-	-	-	-	-	-
Sc II 5527	BA	-	-	-	-	-	-	-	-	-	5434.9(5.5)	79.7(14.5)	0.48(0.90)	5477.2(3.6)	71.7(17.4)	0.85(0.12)	5474.2(27.8)	181.0(50.7)	0.53(0.19)
Sc II 5658	BA	-	-	-	-	-	-	-	-	-	-	-	-	5624.6(4.4)	87.4(28.1)	1.74(0.40)	5638.8(6.8)	111.4(11.6)	0.63(0.16)
CIII 5696	NE	5710.1(1.2)	12.5(1.3)	0.21(0.03)	-	-	-	-	-	-	-	-	-	-	-	-	-	-	-
He I 5876	BE[d]	-	-	-	-	-	-	-	-	-	-	-	-	5913.4(7.6)	92.7(20.3)	1.73(0.60)	-	-	-
	NE	5892.1(1.2)	8.50(0.8)	0.16(0.02)	5885.4(0.6)	10.2(1.2)	0.19(0.08)	5894.5(0.8)	8.8(1.8)	0.22(0.08)	-	-	-	-	-	-	-	-	-
	BA [e]	-	-	-	-	-	-	-	-	-	5806.5(3.1)	91.3(9.1)	2.53(0.21)	5823.1(10.5)	115.2(30.2)	3.84(1.30)	5807.9(3.5)	133.9(24.6)	1.14(0.30)
	NA	-	-	-	5894.5(0.4)	9.9(1.7)	0.25(0.06)	5886.9(1.2)	8.3(2.7)	0.13(0.04)	5886.1(1.3)	11.8(1.9)	0.28(0.06)	-	-	-	-	-	-
??	BA	-	-	-	-	-	-	-	-	-	-	-	-	6081.9(5.2)	93.8(12.5)	0.64(0.16)	6065.5(3.0)	148.4(12.5)	0.64(0.14)
Sc II 6245	BA	-	-	-	-	-	-	-	-	-	-	-	-	6201.7(2.8)	51.9(12.4)	0.36(0.11)	6210.3(5.0)	68.7(16.8)	0.16(0.06)
Si II 6355	BA	-	-	-	-	-	-	-	-	-	6286.8(2.3)	81.7(11.6)	2.49(0.51)	-	-	-	-	-	-
Hα	BE	6579.4(5.2)	97.5(15.7)	5.7(0.9)	6592.9(1.7)	27.1(8.2)	0.54(0.17)	6599.5(10.0)	37.7(15.5)	0.91(0.35)	-	-	-	6571.1(5.3)	149.0(9.1)	17.42(0.72)	6581.7(3.2)/6602.6(3.2)[f]	-	11.27(0.90)
	NE	6581.6(2.6)	11.9(1.9)	1.44(0.22)	6582.4(0.5)	7.9(0.4)	0.58(0.08)	6580.3(2.3)	12.7(4.2)	0.76(0.23)	6582.5(0.9)	7.6(1.3)	0.27(0.07)	6585.3(1.1)	5.8(1.1)	0.16(0.06)	-	-	-
	BA	-	-	-	6553.5(5.4)	215(30.0)	8.22(3.2)	6526.4(15.5)	132.0(16.7)	3.59(0.5)	6486.5(1.6)	90.1(13.1)	1.77(0.38)	-	-	-	-	-	-
	NA	-	-	-	6572.1(1.8)	6.4(2.0)	0.19(0.07)	6574.9(2.3)	9.7(3.5)	0.61(0.35)	6575.0(0.9)	12.3(1.5)	0.51(0.08)	6579.8(5.8)	9.1(3.5)	0.14(0.06)	-	-	-
He I 6678	NE	6696.7(1.3)	8.7(3.0)	0.08(0.02	-	-	-	-	-	-	-	-	-	-	-	-	-	-	-
He I 7065 + CI 7100	BE	7101.3(5.2)	129.9(18.2)	2.78(0.52)	-	-	-	-	-	-	-	-	-	-	-	-	-	-	-
He I 7065	NE	-	-	-	7086.0(0.7)	10.0(1.6)	0.14(0.02)	-	-	-	-	-	-	-	-	-	-	-	-
He I 7065	BA	-	-	-	-	-	-	-	-	-	-	-	-	6935.0(4.6)	110.1(10.6)	1.07(0.10)	-	-	-
Ca II 7291/7324	BE	-	-	-	-	-	-	-	-	-	-	-	-	7326.3(2.6)	67.8(14.3)	0.41(0.13)	7313.8(4.5)	110.6(10.2)	0.73(0.11)
	BA	-	-	-	-	-	-	-	-	-	-	-	-	7250.7(2.9)	26.4(6.1)	0.09(0.03)	-	-	-
O I 7773 + S I 7725	BE	-	-	-	-	-	-	-	-	-	-	-	-	7806.8(10.4)	87.3(9.9)	0.84(0.22)	7796.8(12.5)	86.6(15.5)	0.17(0.04)
He II 8236(?)	BE	8240.6(7.8)	104.2(18.8)	17.20(7.10)	-	-	-	-	-	-	-	-	-	-	-	-	-	-	-
O I 8446+Ca II 8498 [g]	BE	-	-	-	-	-	-	-	-	-	-	-	-	8494.9(3.3)/	-	14.6(1.1)	8522.1(25.6)/	-	8.74(0.90)
Ca II 8542 , Ca II 8662		-	-	-	-	-	-	-	-	-	-	-	-	8674.5(3.3)	-	-	8664.7(30.6)	-	-
O I 9261 + S I 9222	BE	-	-	-	-	-	-	-	-	-	-	-	-	9252.4(2.1)	84.7(10.6)	1.32(0.30)	-	-	-

NOTE.–Values for the FWHM and flux are dependent on both the continuum placements and the deblending procedure, especially in cases of heavy line blending. The errors are given in brackets.

[a] Line shape, "BE"=Broad Emission, "NE"=Narrow Emission, "BA"=Broad Absorption, "NA"=Narrow Absorption

[b] in units of 10^{-13} ergs $cm^{-2}sec^{-1}$. The absorption line fluxes indicate the flux "subtracted" from the continuum.

[c] This is a blend of He II 4686 and C III 4648/ N III 4640.

[d] This is a blend of He I 5876, Ba II 5874 and Na I D lines.

[e] This is a blend of He I 5876, Ba II 5874 and Na I D lines.

[f] This profile is complex and can not be fitted with a single Gaussian. So we measured the flux by integrating the spectra directly. Two narrow "peaks" are superimposed on the broad emission profile at 6581.0(3.5) Å and 6606.7(3.5) Å.

[g] This profile has two clear separate peaks at the wavelengths quoted above. The line flux is measured for the whole feature. Separation of the different components of the Ca II IR triplet (Ca II 8498, 8542 , 8662) and of O I 8446 was not performed due to the close blend of these lines.

with SN 1998S. It therefore seems unlikely that these two lines originate in the SN CSM. We also note that in table 4 of Bowen et al., 'He I 4290 Å' should probably be read as 'He I 4920 Å'. Bowen et al. also list a narrow P Cygni line identified with He I 4713 Å. While there is a weak feature at this wavelength in our reduced data, its S/N is very low and so we do not include it in Table 5. Narrow optical lines identified by us but not listed by Bowen et al. include He I 6678, 7065 Å and [Fe III] 4658 Å.

The forbidden lines on day 36.3 all exhibit about the same absolute redshift and width (see below), with a weighted mean redshift of $+846.9 \pm 2.9\,\mathrm{km\,s^{-1}}$. We adopt this as probably being closest to the SN centre-of-mass redshift, for the following reasons. We note below that between days 17.4 and 36.3 the red wings of the emission components of the H lines (and possibly also the He I lines) and forbidden lines moved to the red by $\sim+10$–$20\,\mathrm{km\,s^{-1}}$. We suggest that this is a manifestation of light travel time effects across the CSM around the supernova. The radius of the outer CSM is at least 10 light days (see below), and so on the time-scale of the observations as the SN-flash paraboloid moves further into the CSM on the far side of the SN, increasing amounts of more redshifted material will contribute to the emission lines. We therefore favour the later epoch (day 36.3) since by that time the emission lines should be originating from a greater proportion of the CSM, i.e., the bias to the blue due to light travel time effects should be reduced. We also favour the forbidden lines, since the allowed lines appear to be considerably more complex, comprising a mixture of broad and narrow P Cygni components plus a probable additional recombination emission component. Our adopted redshift for the supernova CSM, $+847\,\mathrm{km\,s^{-1}}$, is consistent with the approximate value of $+860\,\mathrm{km\,s^{-1}}$ indicated in Bowen et al. (2000). We note that measurements of the systemic velocity of NGC 3877 vary from $+838 \pm 11\,\mathrm{km\,s^{-1}}$ using optical observations of the nuclear region (Fouqué et al. 1992; Ho, Filippenko & Sargent 1995), to $902 \pm 6\,\mathrm{km\,s^{-1}}$ (de Vaucouleurs et al. 1991) and $+910 \pm 6\,\mathrm{km\,s^{-1}}$ (Broeils & van Woerden 1994) using an H I 21-cm emission-line map.

We have examined variations in shifts, widths and intensities of the stronger narrow lines between different species and epochs. The lines considered were Hα, β, γ, He I 4471, 5015, 5875 Å, [O III] 4959, 5007 Å, [N II] 5755 Å, [Ne III] 3869 Å and [Fe III] 4658, 5270 Å. In Fig. 11 we show in detail those lines which were detected on both days 17.4 and 36.3, viz. H, He I and [O III]. The relative velocity shifts discussed below are with respect to our adopted SN centre-of-mass velocity of $+847\,\mathrm{km\,s^{-1}}$.

The following general conclusions can be reached. Where the S/N was sufficiently high, we can say that the peaks and troughs of the H and He lines exhibited similar velocity shifts with respect to the SN centre-of-mass frame. On day 17.4, their emission peaks were at $+8 \pm 3\,\mathrm{km\,s^{-1}}$, moving to $+15 \pm 3.5\,\mathrm{km\,s^{-1}}$ on day 36.3. The red wings of the H lines appear to shift to the red by around $15\,\mathrm{km\,s^{-1}}$ between the two epochs. Similar behaviour may be apparent in some of the He I lines also. In contrast, the absorption troughs (which also showed no difference in velocity shift between H and He) remained at a mean shift of $-25 \pm 3\,\mathrm{km\,s^{-1}}$ between the two epochs. The blue extremities of the H lines extended to $\sim-55\,\mathrm{km\,s^{-1}}$ on both epochs, whereas the blue limit of the He I lines was $\sim-40\,\mathrm{km\,s^{-1}}$. The red extremities of the H and He I lines lay at $\sim+60\,\mathrm{km\,s^{-1}}$, apart from H$\alpha$ which reached about $+90\,\mathrm{km\,s^{-1}}$. Fig. 11 also reveals that the absorption component in most of the H and He I lines became significantly deeper, while the emission component showed a much smaller intensity variation. Only in Hα did the depth of the absorption remain about the same. (This may also apply to He I 4471 Å, but the S/N is very low.) On day 17.4, the only detectable forbidden lines were those of [O III], and only [O III] 5007 Å was of good S/N.The blue edge of this line lay at $\sim-40\,\mathrm{km\,s^{-1}}$, similar to that of the He I lines. However, the red edge extended no further than $+15\,\mathrm{km\,s^{-1}}$. By day 36.3, the blue edge remained at $-40\,\mathrm{km\,s^{-1}}$, but the red edge had moved to $\sim+40\,\mathrm{km\,s^{-1}}$. As mentioned above, we suggest that this is due to light travel time effects. By this epoch, lines of [N II], [Ne III] and [Fe III] were also measurable, and these all showed about the same absolute redshift and width as the [O III] lines. The [O III] profiles showed little variation in peak flux between the two epochs.

In summary, the red wings of most of the emission lines showed a movement to the red of around $+10$ to $+20\,\mathrm{km\,s^{-1}}$ between the two epochs, while the blue limits of the forbidden-line emission profiles and the allowed-line absorption profiles remained roughly stationary, i.e., the extent of the lines effectively increased by $+10$ to $+20\,\mathrm{km\,s^{-1}}$ between the two epochs due the redshift of the red wing. We attribute this to light travel time effects. We also note that the fact that the [O III] 5007-Å profile varies in time, together with the similarity of its shape and redshift on day 36.6 to those of other forbidden lines, indicates that the SN CSM is indeed the origin of these lines. This rules out the alternative line-of-sight emission-line region suggested by Bowen et al. (2000).

The narrow P Cygni lines of He I 10 830 Å acquired at UKIRT (resolution $\sim100\,\mathrm{km\,s^{-1}}$) on days 44 and 55 are also listed in Table 5. The emission profiles and peak–trough profiles are unresolved. The emission peak lies at velocities of $+29 \pm 20\,\mathrm{km\,s^{-1}}$ on day 44 and $-7 \pm 15\,\mathrm{km\,s^{-1}}$ on day 55, which are the same as for the optical He I lines, to within the uncertainties. The line strengths are virtually identical at the two epochs. While the main emission and absorption components are unresolved, there is some indication that the blue wing of the absorption is barely resolved, reaching a blueshift of $\sim-300\,\mathrm{km\,s^{-1}}$, i.e., similar to that found for the wing of the broad Hα absorption.

We conclude that the narrow lines arose in a CSM wind of velocity of 40–60 $\mathrm{km\,s^{-1}}$. The highest velocities ($\sim60\,\mathrm{km\,s^{-1}}$) are seen in the H lines, and the lowest ($\sim40\,\mathrm{km\,s^{-1}}$) in the forbidden lines. The greater velocity extent of the H lines may be in part due to the stronger effects of thermal broadening in this element. For a temperature of 10 000 K, the thermal broadening contribution has a FWHM of $21\,\mathrm{km\,s^{-1}}$ in hydrogen compared with just $5\,\mathrm{km\,s^{-1}}$ in oxygen. It is also possible that radiative acceleration effects could contribute to the greater width of the allowed lines. Acceleration of the CSM could be driven by the UV radiative precursor and/or cosmic ray precursor (Fransson, Lundqvist & Chevalier 1996), with the innermost part of the CSM being accelerated most. The optical depth in allowed lines in the accelerated CSM component could be large (due to high radiative excitation), thereby increasing the width of the scattered lines. However, it is quite plausible that the volume emission measure of the accelerated component is low, and so would not contribute to the forbidden lines.

Turning briefly to the broader absorption component in the optical H and He I lines, we can see (Fig. 11) that this feature strengthened somewhat between days 17.4 and 36.3. Similar behaviour is reported for the H lines by Bowen et al. (2000). However, Bowen et al. also note the presence of a similarly broad absorption in Mg II 2796, 2803 Å, which (a) may have *declined* in strength between days 32 and 39, and (b) never exhibited narrow P Cygni lines. We also note that the Hα and Hβ lines are

Table 4. Line identifications for the infrared spectra of SN 1998S.

DAY	ID	λ_{peak}(Å) (Emis.)	λ_{peak}(Å) (Absorp.)	LS[a]	FWHM (Å)	FLUX[b]
2.8	Br_δ	19 470(20)		BE	220(55)	0.85(0.25)
	Br_δ	19 494(6)		NE	29(8)	0.1(0.05)
	Br_γ	21 775(35)		BE	380(90)	0.3(0.1)
	Br_γ	21 735(6)		NE	45(15)	0.06(0.03)
4.8	He I 10 830 + P_γ	10 910(15)		BE	241(35)	13.9(3.1)
	P_γ	10 966(8)		NE	32(8)	0.8(0.3)
	He I 10 830	10 869(8)		NE	32(8)	1.3(0.2)
	He II 11 626?	11 653(10)		BE	110(25)	4.0(0.8)
	P_β	12 846(20)		BE	153(42)	6.1(1.5)
	P_β	12 847(8)		NE	38(8)	1.4(0.4)
6.8	He I 10 830 + P_γ	10 930(20)		BE	210(22)	14.9(1.9)
	He I 10 830	10 875(5)		NE	29(4)	1.8(0.3)
8.9	Br_δ	19 469(20)		BE	133(40)	1.1(0.3)
	Br_γ	21 726(20)		BE	115(25)	0.5(0.1)
11.9	He I 10 830		10 850(5)	NA	26(7)	2.1(0.6)
	He I 10 830	10 874(5)		NE	50(10)	3.1(0.9)
	He I 10 830 + P_γ	10 950(20)		BE	126(20)	6.9(0.6)
	P_γ	10 973(4)		NE	17(5)	0.4(0.2)
	P_β	12 868(10)		BE	101(20)	3.2(0.5)
	P_β	12 864(4)		NE	26(7)	0.7(0.3)
12.8	Br_δ	19 470(30)		BE	96(25)	0.5(0.2)
	Br_δ	19 497(12)		NE	23(8)	0.10(0.04)
	Br_γ	21 770(25)		BE	225(65)	0.35(0.15)
	Br_γ	21 729(6)		NE	35(15)	0.13(0.04)
17.7	He I 10 830		10 856(4)	NA	27(9)	2.1(0.8)
	P_γ	10 975(4)		NE	23(9)	0.7(0.4)
	He I 10 830	10 872(2)		NE	25(6)	1.7(0.4)
	He I 10 830 + P_γ	10 945(20)		BE	170(40)	7.5(2.5)
	P_β	12 855(5)		NE	21(8)	0.5(0.2)
	P_β	12 858(25)		BE	150(50)	3.0(1.2)
44.6	He I 10 830 + P_γ		10 642(30)	BA	226(35)	11.0(2.5)
	He I 10 830 + P_γ	10 915(30)		BE	210(35)	30.5(5.5)
	He I 10 830		10 852(5)	NA	23(0.5)	0.25(0.08)
	O I 11 287/11 294 +S I 11 306	11 300(15)		BE	150(25)	5.8(0.7)
	Si II 12 047 +Mg I 11 828	11 935(11)		BE	280(15)	14.5(1.9)
	P_β	12 817(10)		BE	216(15)	17.9(1.5)
	Mg I 15 031	15 027(15)		BE	105(30)	2.1(0.4)
	O I 18 243/18 021	18 196(26)		BE	300(45)	2.7(0.4)
	P_α	18 763(20)		BE	341(30)	16.7(1.5)
	P_α	18 749(4)		NE	34(6)	0.65(0.15)
	Br_δ	19 460(20)		BE	285(40)	3.5(0.6)
	Br_γ	21 690(25)		BE	335(40)	3.3(0.4)
55.5	P_δ	10 045(10)		BE	205(35)	14.9(5.0)
	P_δ		10 044(4)	NA	25(9)	1.7(0.6)
	He I 10 830 + P_γ		10 600(20)	BA	130(30)	8.5(1.8)
	He I 10 830		10 851(5)	NA	17(8)	1.4(0.5)
	He I 10 830 + P_γ	10 910(20)		BE	205(35)	41.2 (1.9)
	O I 11 287/11 294 +S I 11 306	11 300(10)		BE	165(35)	10.0(2.5)
	Si II 12 047 +Mg I 11 828	11 950(20)		BE	345(40)	18.0(1.7)
	P_β	12 825(15)		BE	205(25)	29.5(2.5)
108.6-126.6	He I 10 830 + P_γ	10 910(15)		BE	275(25)	35.0(7.0)
	O I 11 287 +S I 11 306	11 327(15)		BE	250(30)	14.5(3.5)
	Si II 12 047 +Mg I 11 828	12 017(37)		BE	330(55)	6.5(2.0)
	P_β	12 875(15)		BE	300(30)	20(2.5)
	Mg I 15 031	15 053(20)		BE	208(35)	2.3(0.4)

Table 4 – *continued*

DAY	ID	λ_{peak}(Å) (Emis.)	λ_{peak}(Å) (Absorp.)	LS[a]	FWHM (Å)	FLUX[b]
	Br series, Si I 15 888, [Fe II], [Si I], Mg I	BLEND		BE	–	9.8(2.5)[c]
	P_α	18 833(40)		BE	430(50)	33.5(6.5)
	Ca I 19 309–19 961	19 585(65)		BE	480(90)	6.7(2.5)
	Br_γ	21 770(45)		BE	490(85)	3.9(1.2)
	CO	∼23 400		BE	–	>30

NOTE.-Values for the FWHM and flux are dependent on both the continuum placement and the deblending procedure, especially in cases of heavy line blending. The errors are given in brackets.
[a] Line shape, 'BE' = Broad Emission, 'NE' = Narrow Emission, 'BA' = Broad Absorption, 'NA' = Narrow Absorption.
[b] in units of 10^{-14} erg cm^{-2} s^{-1}. The absorption-line fluxes indicate the flux 'subtracted' from the continuum.
[c] This is the integrated flux from 15 500–17 700 Å.

sufficiently well defined to allow us to conclude that the broad minima were blueshifted by ~ -115 km s^{-1} on day 17.4, moving redward to ~ -85 km s^{-1} by day 36.3.

4 DISCUSSION

4.1 The circumstellar medium of SN 1998S

The CSM of SN 1998S has been described and discussed by a number of authors (L00; G00; Fassia et al. 2000, Bowen et al. 2000, Lentz et al., in preparation). In the following discussion we adopt the general consensus about the form of the CSM and the evolution of the spectra. In particular, we confirm the two-phase CSM proposed by L00, but we deduce somewhat different, and occasionally firmer, constraints on the size and density of the CSM. In this paper we focus mostly on what can be deduced from the first-season observations. Later observations will be described in a subsequent paper (Fassia et al., in preparation). We envisage that before it exploded, the progenitor star of SN 1998S had undergone two phases of mass-loss, with a gap or a phase of reduced mass-loss in between. This gave rise to two shells of CSM. Following L00, we shall refer to these as the inner CSM (ICSM) and the outer CSM (OCSM). The interaction of the ejecta with these two shells is responsible for the early ($t < 10$ d) and late ($t > 40$ d) time appearance of broad emission lines lacking a P Cygni absorption component (cf. Chevalier & Fransson 1994; Chugai & Danziger 1994).

4.1.1 The inner circumstellar material (ICSM)

We recall that the early-time broad component had a FWHM ≥ 4000 km s^{-1}, was present as early as day 3, and had faded significantly by days 12–14 (Qiu et al. 1998; this paper). While lines of this width in SNe are usually associated with the ejecta, the absence of any corresponding P Cygni absorption is a robust indicator that these lines are driven by the high-energy radiation of the shock resulting from the interaction of the ejecta with dense CSM in the immediate vicinity of the supernova (Chugai 1990). The ratio of the luminosities of the Hα and Hβ broad components in the first week spectra is $f_{H\alpha}/f_{H\beta} = 1.45 \pm 0.25$ and the ratio of the fluxes of the Pβ and Hγ lines is $f_{P\beta}/f_{H\gamma} = 0.22 \pm 0.07$. If we take into account the reddening, assuming $A_V = 0.68^{+0.34}_{-0.25}$ (Fassia et al. 2000), then these ratios become $f_{H\alpha}/f_{H\beta} = 1.1 \pm 0.7$ and $f_{P\beta}/f_{H\gamma} = 0.1 \pm 0.06$. These low ratios indicate a high degree of thermalization for these lines, and thus imply a high density and a large optical depth for the line-forming region.

The fading of the broad emission components by days 12–14.3 and the appearance of broad absorption components in H and He I by days 14.3–17.7 (cf. Fig. 7) is strong evidence that by that time the ejecta had completely overrun the ICSM. The highest ejecta velocity was about $\sim 10\,000$ km s^{-1} relative to the SN centre of mass. We therefore estimate that the outer limit of the ICSM was ≤ 90 au. By day ~ 15 the photospheric radius was already ~ 75 au (Fassia et al. 2000).

4.1.2 The region between the ICSM and OCSM

As can be seen in Figs 7 and 8 the spectra during days 14–27 are dominated by broad P Cygni-type absorption profiles. During this phase, the extreme blue edge of the broad absorption indicated a velocity of -8000 km s^{-1} relative to the SN centre of mass. We adopt this as the maximum velocity of the ejecta. The ejecta collided with the OCSM sometime after day 27. The high-resolution spectra of day 36 show no sign of broad emission. However, by day 44, strong broad emission had appeared in the IR lines. We deduce that the 8000 km s^{-1} shock reached the inner edge of the OCSM on day 40 ± 4, indicating a radius of 185 ± 20 au. So the region between the ICSM and OCSM extended from ≤ 90 au to ~ 185 au.

There is evidence that even during the phase when the ejecta had overrun the ICSM but not yet reached the OCSM, the ejecta/CSM interaction contributed significantly to the spectrum. While the SN 1998S spectral lines at this phase are similar to those observed in the spectra of normal SNe II during their photospheric phase (e.g. Blanton et al. 1995; Fassia et al. 1998), the SN 1998S spectrum differs in that it has a much stronger, bluer continuum and shallower absorption profiles. As mentioned in Section 3.1.3, Branch et al. (2000), Lentz et al. (in preparation) and L00 suggest that the low contrast of the broad lines relative to the continuum is due to external illumination of the line-forming region by light from the CSM–ejecta interaction. We agree with this suggestion, and furthermore propose that the observed strong continuum emission arises in a massive, cool, dense shell of ejecta formed at the ICSM–ejecta discontinuity (e.g. Chevalier & Fransson 1994). Such a shell is likely to be produced by the interaction of the ejecta with the ICSM, and would have a velocity jump of

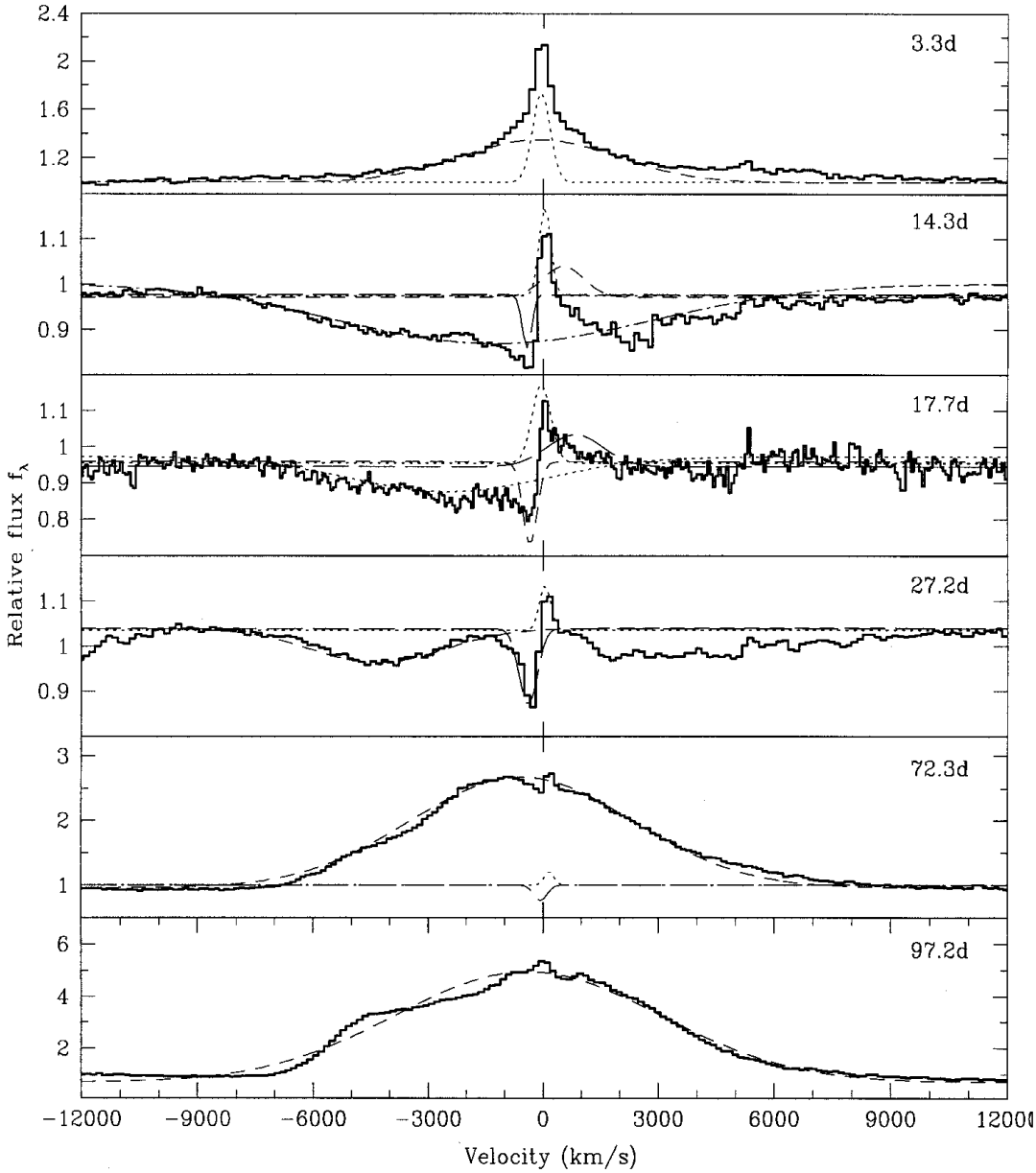

Figure 9. Evolution of the Hα line profile. Also shown are the Gaussian components that were used to fit the observed line profiles. The 0 km s^{-1} velocity corresponds to the adopted +847 km s^{-1} velocity for the SN centre of mass (see Section 3.2).

$\sim 10^3$ km s^{-1} between the inner part of the ejecta and the shell. This could have led to enhanced continuum emission in two ways. In the first mechanism, even after the ejecta have completely overrun the ICSM, the existence of the velocity jump would have resulted in a reverse shock wave which ran through the ejecta and which would have remained powerful enough to generate strong continuum emission from the dense shell. For the second mechanism, we suppose that between the ICSM and the OCSM there actually existed a tenuous, uniformly distributed circumstellar medium, which we shall to refer to as the MCSM (mid-CSM). Interaction of the dense, swept-up shell with the MCSM would have released power (kinetic luminosity) according to $L = 2\pi R^2 \rho v^3$ or $L \propto R^2 \propto t^2$. Interestingly, between days 17.7 and 44.6 the Pβ flux grew $\sim$6 times, in good agreement with the expansion factor between these two epochs, viz. $(t_2/t_1)^2 = 6.3$. We note, however, that if the Pβ lines arose from the dense shell and were thermalized (saturated) at a constant excitation temperature, then the expansion of the dense shell alone could account for the $L \propto R^2$ behaviour. Nevertheless, if the dense shell did exist, then it may have contributed to the broad-line emission which appeared in the IR by day 44, i.e., at this epoch the line luminosities may have been composed of contributions from both radioactive and ejecta/CSM energy sources, where 'CSM' includes ICSM, MCSM and OCSM. However, determination of the relative luminosities from these sources, and what fraction of the ejecta/CSM luminosity arose from the different zones, is beyond the scope of this paper.

4.1.3 The outer circumstellar material (OCSM)

The presence of the OCSM is revealed in two phases. The earlier

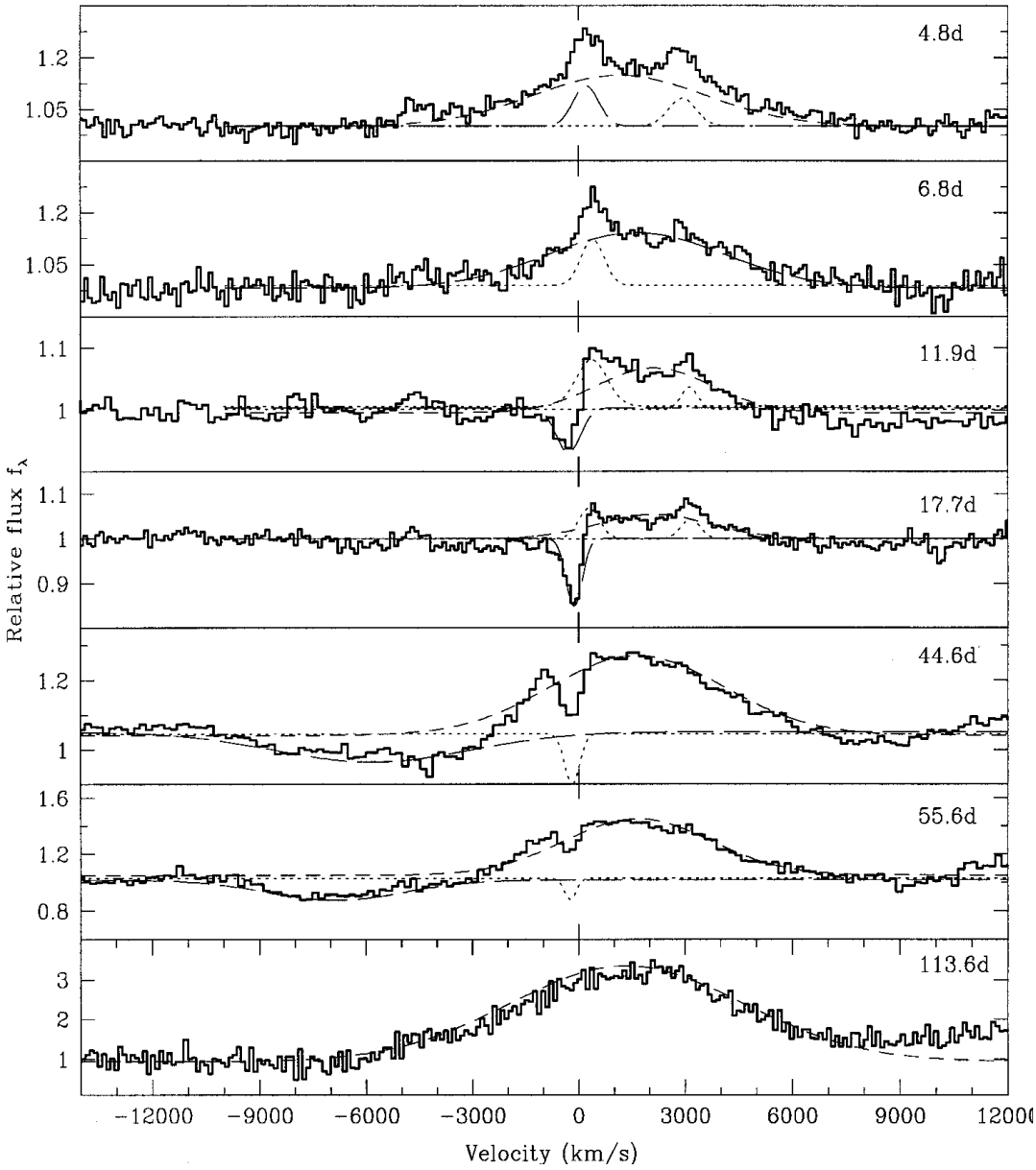

Figure 10. Evolution of the He I 10 830 line profile. Also shown are the Gaussian components that were used to fit the observed line profiles. The 0 km s^{-1} velocity corresponds to the adopted +847 km s^{-1} velocity for the SN centre of mass (see Section 3.2).

is due to its interaction with the UV/X-ray flash from the SN, and the later is due to its interaction with the SN ejecta.

4.1.3.1 The early phase. We attribute the early, narrow, usually unresolved, lines to recombination and heating following ionization of the slowly moving OCSM by the UV/X-ray flash at shock break-out. These lines were present in the earliest spectra (day 3.3) as the narrow (FWHM $\leq$ 500 km s^{-1}) components of the emission lines. By days 12–14, the narrow H and He I lines began to take on the form of P Cygni profiles, and this is clearly confirmed in the day 17.4 WHT/UES spectra. However, the high-resolution spectra also show that the narrow lines in H and He I are actually made up of at least two components. The components are best described as a P Cygni-like profile of maximum velocity ~50–60 km s^{-1} and a broader, blueshifted absorption extending to around −350 km s^{-1}. The high-resolution spectra also show narrow forbidden lines extending to ±40 km s^{-1} of the centre-of-mass velocity.

We consider first the narrowest lines or line components, i.e., those extending to ±40–60 km s^{-1}. We envisage that the narrow P Cygni-like profiles in H and He I were produced by two effects. The recombination cascade in the OCSM would generate narrow emission lines. In addition, the recombination would populate excited levels in the OCSM, resulting in photospheric photons being resonantly scattered, hence forming classical P Cygni lines. Thus the narrow-line emission component comprises photons emitted both through recombination and resonant scattering. We note that the He I 6678, 7065 Å lines appear only in emission, and only in the day 17.4 spectra. He I 6678 Å is produced by a singlet transition to the $2p^1P_0$ level. The lack of an absorption in this line is presumably due to rapid decay from $2p^1P_0$ to the metastable $2s^1S$ level. In contrast, the 5015-Å line is produced by a transition directly to the $2s^1S$ level, and that accounts for the absorption in this line. Thus He I 6678 Å is a virtually pure recombination line, and its disappearance by day 36.3 is presumably due to a lowering

Table 5. Narrow lines observed at high resolution. All observations were on day 17.4 or 36.3 unless indicated otherwise.

ID[a]	17.4 days Shift[b] (km s^{-1})	17.4 days FWHM (km s^{-1})	17.4 days Flux[c]	36.3 days Shift[b] (km s^{-1})	36.3 days FWHM (km s^{-1})	36.3 days Flux[c]
Emission Lines						
[*Ne* III] 3868.75	–	–	–	+845(11)	55(12)	0.40(0.10)
H8 + He I 3889.843[d]	–	–	–	+866(15)	108(25)	1.67(0.82)
He I 3964.729	–	–	–	+852(15)	72(20)	0.28(0.12)
Hϵ(3970.072)	–	–	–	+867(11)	64(16)	0.74(0.48)
He I 4026.209	–	–	–	+880(13)	37(11)	0.07(0.03)
Hδ(4101.74)	–	–	–	+859(7)	65(11)	0.84(0.34)
Hγ(4340.47)	859(10)	42(3)	0.79(0.15)	+862(7)	55(3)	0.89(0.03)
[*O* III] 4363.209	–	–	<0.40	+844(10)	65(12)	0.26(0.07)
He I 4471.502	851(18)	60(33)	0.22(0.10)	+865(8)	103(22)	0.65(0.15)
[*Fe* III] 4658.05	–	–	–	+846(10)	39(16)	0.14(0.05)
Hβ(4861.330)	855(5)	43(9)	0.96(0.21)	+862(6)	46(9)	1.54(0.21)
[*O* III] 4958.911	840(5)	30(7)	0.23(0.03)	+845(11)	48(7)	0.22(0.05)
[*O* III] 5006.843	836(5)	48(9)	0.65(0.12)	+847(7)	59(9)	0.65(0.11)
He I 5015.678	847(6)	39(13)	0.19(0.08)	+858(7)	57(16)	1.05(0.25)
[*Fe* III] 5270.40	–	–	–	+868(14)	60(15)	0.17(0.06)
[*N* II] 5754.59	–	–	–	+848(5)	45(3)	0.30(0.04)
He I 5875.661	854(5)	40(3)	0.52(0.07)	+863(5)	42(5)	0.79(0.17)
Hα (6562.799)	855(5)	55(5)	2.15(0.58)	+864(5)	55(7)	2.09(0.04)
Hα[e](6562.799)	–	–	–	+868(5)	50(5)	1.88(0.17)
[*N* II] 6583.45	–	–	–	+843(7)	90(40)	0.09(0.04)
He I 6678.152	851(5)	70(7)	0.44(0.13)	–	–	–
He I 7065.25	855(5)	50(5)	0.43(0.04)	–	–	–
He I 10 830[f]	–	–	–	+876(40)	<100	1.56(0.35)
He I 10 830[g]	–	–	–	+840(40)	<100	0.9(0.30)
Absorption lines						
H8 + He I 3889.843	–	–	–	–41(7)	23(2)	1.11(0.02)
He I 3964.729	–	–	–	−24(4)	16(3)	0.31(0.02)
Hϵ(3970.072)	–	–	–	−23(5)	30(6)	0.69(0.14)
He I 4026.209	–	–	–	−28(8)	27(3)	0.08(0.02)
Hδ(4101.74)	–	–	–	−23(5)	30(13)	0.90(0.08)
Hγ(4340.47)	–	–	–	−22(5)	36(3)	1.13(0.07)
He I 4471.502	−28(8)	13(10)	0.79(0.10)	−23(10)	25(10)	0.27(0.05)
Hβ(4861.33)	−28(5)	25(6)	0.35(0.11)	−26(5)	42(4)	1.78(0.25)
He I 5015.678	−25(4)	16(3)	0.21(0.05)	−21(4)	16(3)	0.87(0.07)
He I 5875.661	−27(4)	15(3)	0.26(0.04)	−25(5)	19(3)	0.61(0.04)
Hα (6562.799)	−26(5)	32(5)	1.19(0.10)	−33(5)	45(14)	1.06(0.44)
Hα[e]	–	–	–	−27(8)	40(10)	0.87(0.07)
He I 10 830[f]	–	–	–	−100(60)	<100	2.28(0.55)
He I 10 830[g]	–	–	–	−100(60)	<100	2.1(0.55)

[a] The rest wavelengths were obtained from the NIST Atomic Spectra Database and the CRC Handbook of Chemistry and Physics, 79th Edition.
[b] For emission lines, the total redshift is given. For absorption lines, the shift is with respect to SN centre of mass (+846.9 km s^{-1}). Errors are given in brackets.
[c] in units of 10^{-14} erg cm^{-2} s^{-1}. The absorption line fluxes indicate the flux 'subtracted' from the continuum. Errors are given in brackets.
[d] We adopted $\lambda = 3888.652$ Å for this blend.
[e] Observed at 38.5 d.
[f] Observed at 44.6 d.
[g] Observed at 55.6 d.

of the recombination rate by then. He I 7065 Å is produced by a triplet transition to the $2p^3P_0$ level. The presence of absorptions in the 5876- and 4471-Å lines (which both also decay to the $2p^3P_0$ level) indicates a significant population in $2p^3P_0$. However, the cross-section for resonant scattering from this level via the 7065-Å transition is only about 10 and 50 per cent relative to that of the 5876- and 4471-Å transitions respectively. Given that the 4471-Å line barely exhibits an absorption component above the noise, it is not surprising that there is little evidence of absorption in the 7065-Å line. The stronger pronounced emission component in 7065 Å relative to 4471 Å may be due to its being of lower excitation energy. Collisional excitation from the metastable $2s^3S$ level would thus be expected to produce a significantly stronger 7065-Å line. The disappearance of the 7065-Å line by day 36.3 is probably due to cooling of the electron gas. The forbidden lines would have been excited as a result of the heating of the OCSM electron gas following recombination. The appearance of narrow [N II], [Ne III] and [Fe III] lines between days 17.4 and 36.3 can be attributed to the formation of the relevant species following recombination from higher ionization.

We can estimate the CSM density in the region where the [O III] lines were formed by using the ratio of their fluxes $R = (f_{\lambda 4959} + f_{\lambda 5007})/f_{\lambda 4363}$. L00 measured the ratio of the narrow [O III] lines present in their day 4 and day 5 spectra, and found that for

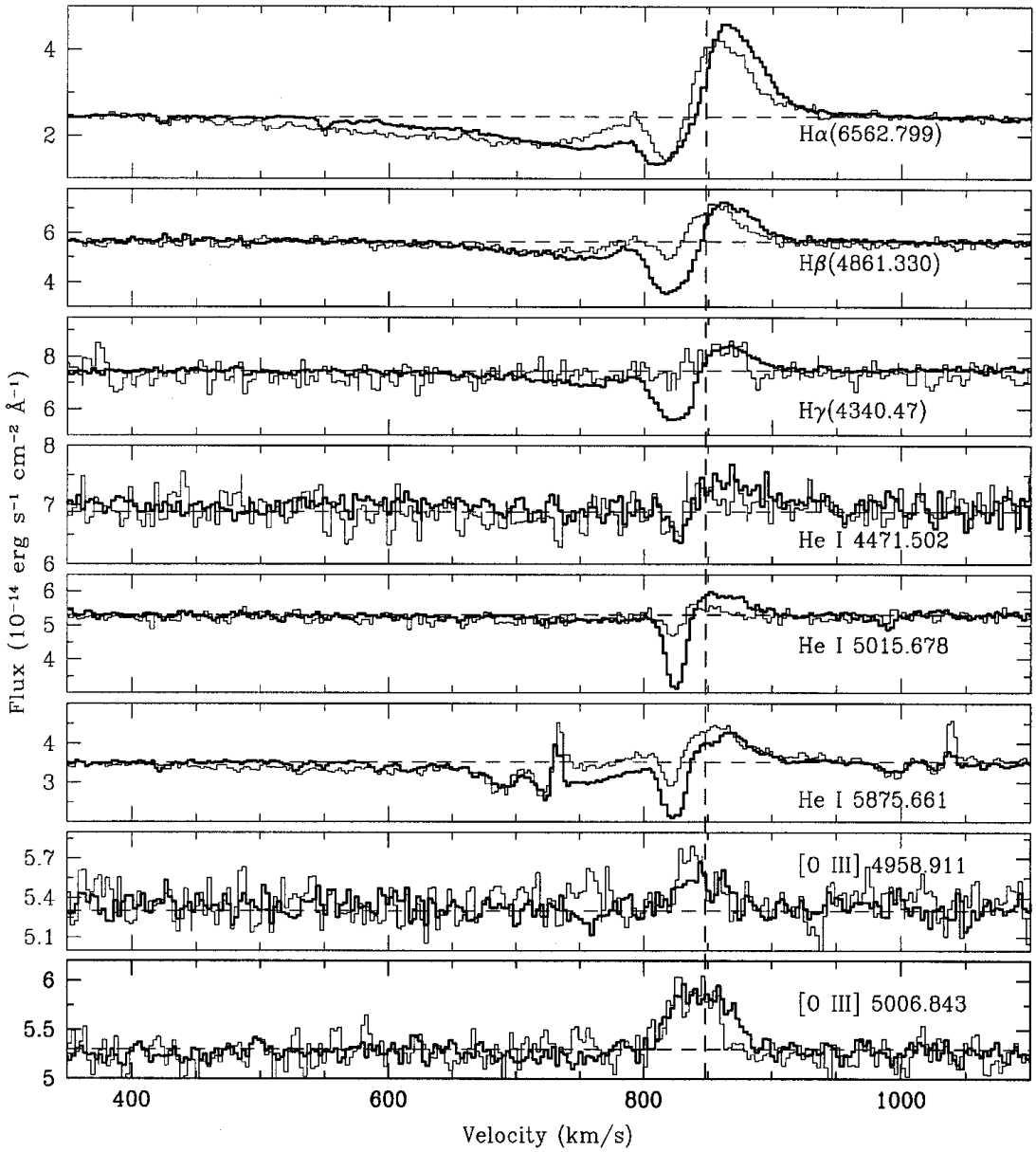

Figure 11. Narrow line profiles observed in the day 17.4 (fainter line) and day 36.3 (darker line) high-resolution spectra. The vertical dashed line corresponds to the adopted redshift for the SN centre of mass, 847 ± 3 km s^{-1} (cf. Section 3.2). To help the comparison of the line profiles, the day 36.3 continua have been displaced vertically to coincide with the day 17.4 continua.

temperatures in the range $15\,000 < T < 30\,000$ K the electron density of the CSM was $6 \times 10^6 < n_e < 2 \times 10^7$ cm^{-3}. However, the SPSDAS package of IRAF that they use to derive these values is appropriate only for a low-density ($n \lesssim 10^5$ cm^{-3}) plasma. In addition, theoretical models developed to study the temperature and structure of the CSM around supernovae (Lundqvist & Fransson 1988) have shown that the CSM temperature is very sensitive to the ionizing spectrum of the supernova, and varies both with radius and in time. The temperature range considered by L00 for the O III-rich gas is much narrower than in the models of Lundqvist & Fransson, which indicate 10^4–10^5 K for a distance greater than ~200 au in a situation similar to that of SN 1998S. The upper limit, 10^5 K, is set by the fact that O III is collisionally ionized to O IV at higher temperatures.

To calculate the CSM density from the [O III] line ratio, we therefore assumed that $10^4 < T < 10^5$ K, and used the six-level [O III] model atom described in Maran et al. (2000). This model includes O III atomic data from Aggarwal (1993) and Galavis, Mendoza & Zeippen (1997), and takes into account collisional de-excitation that plays an important role for $n \gtrsim 10^5$ cm^{-3}. Unfortunately, our day 3.3–17.7 low-resolution spectra are of insufficient S/N for us to estimate the ratio, R, of the oxygen lines. However, we were able to estimate the ratio on day 36.3 using our high-resolution observations. Before dereddening, the ratio is $R = 3.3 \pm 1.0$. Dereddening using the Cardelli et al. (1989) law with $A_V = 0.68^{+0.34}_{-0.25}$ (Fassia et al. 2000) changes the ratio to $R = 2.9 \pm 1.5$. Therefore, using the six-level model atom mentioned above, we estimate that for $1.4 < R < 4.4$ the lower limit to the CSM density is 1×10^6 cm^{-3}. A CSM of this density and velocity (40–50 km s^{-1}) is consistent with it being a red supergiant wind

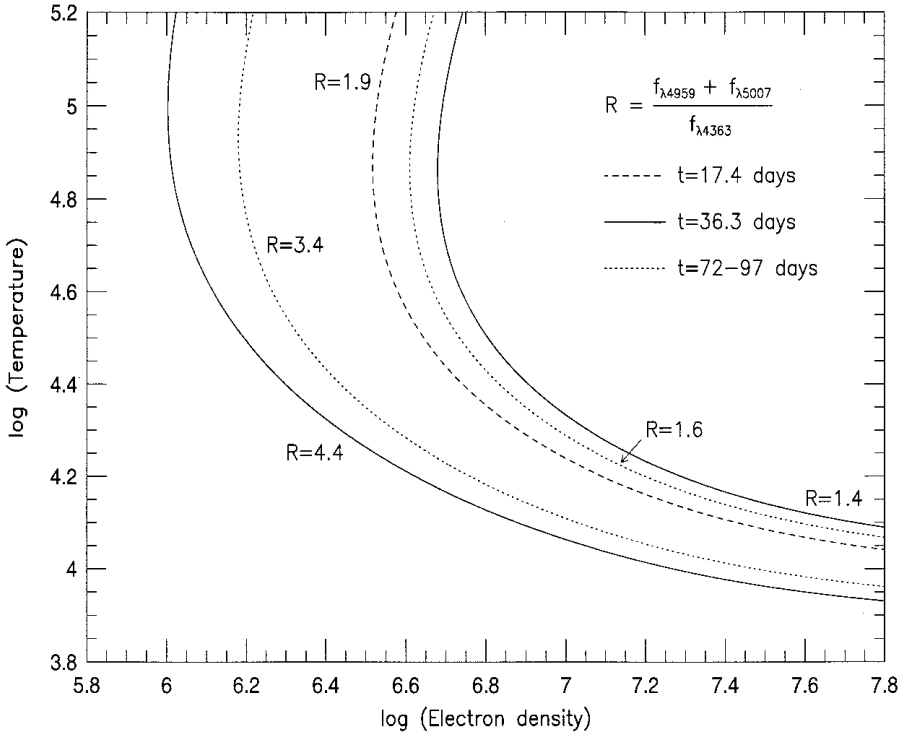

Figure 12. Solutions of the six-level model atom for values of the [O III] line ratio, R, estimated from the SN 1998S spectra (cf. Section 4.1.3).

(Dupree 1986; Jura & Kleinmann 1990; Salasnich, Bressan & Chiosi 1999). No solution for the density is found for $T \leq 8000$ K (see Fig. 12), which means that this is a firm lower limit to the temperature in the O III-rich gas at this epoch. If the temperature is $T \leq 11\,000$ K, which cannot be excluded from the results of Lundqvist & Fransson (1988), no upper limit to the density can be given. The day 36.3 line ratio therefore places only lower limits on the density and temperature of the O III-rich gas.

For day 17.4, only an upper limit is available for the flux of [O III] 4363 Å from our high-resolution spectra, and so we get $R > 1.9$ (dereddened). From Fig. 12 we see that this, unfortunately, does not constrain the density for the temperature range 10^4–10^5 K.

We turn now to the broader ($\sim$350 km s^{-1}) shallower absorption component seen in the H and He I lines. We recall that this feature deepened between days 17.4 and 36.3. The minima also moved redward from ~ -115 to ~ -85 km s^{-1}. The discrete difference in its FWHM, relative to that of the narrow component, might indicate that the two components were formed in different regions. The presence of the broader absorption as late as day 35 implies that it too must have arisen in the OCSM. It could not have been due to the ICSM, since it had been totally overrun by then. In addition, an origin in the region between the ICSM and OCSM seems unlikely, since not only must the density of material there have been quite low (see above), but also by day 35 the undisturbed region between the shock and the inner edge of the OCSM was very thin – barely $\sim$25 au. While a wind velocity $\sim$350 km s^{-1} is too high for a red giant, blue supergiant (BSG) winds do exhibit velocities in the range $\sim$100 to $\sim$3000 km s^{-1} (e.g. Abbott et al. 1981). Thus a possible explanation for the broader absorption is that it occurred in a component of the OCSM produced when the progenitor was going through a BSG phase. The deepening and shift to the red suggest that the effect of a BSG wind 'piling up' against the inner boundary of the RSG wind. This would produce a negative velocity gradient in the BSG wind, as well as making its density gradient less steep. As the SN shock progressed, it would first engulf the faster, more tenuous part of the BSG wind, leaving the outer, slower-moving zone undisturbed, thus accounting for the decrease in the absorption blueshift. The deepening absorption could be due to an increase in the density of the outer, slower-moving zone of the BSG wind as it became increasingly compressed between the shock and the RSG wind boundary. The division of the OCSM into two zones in this scenario would also provide a natural explanation for the apparently discrete difference in the FWHM of the narrower and broader absorption features.

A possible alternative explanation for the $\sim$350 km s^{-1} absorption component is that it might be produced by the acceleration of the innermost OCSM by the radiation pressure of the UV precursor, mentioned at the end of Section 3.3. This would also produce the required negative velocity gradient. Details of the physics of the high-velocity wind component will be considered in a separate paper.

4.1.3.2 The later phase As indicated above, we take the presence of strong, broad Paschen and Brackett lines on day 44 to imply that the shock/OCSM interaction had already already begun by this date. This is further supported by the weakening of the narrow components of the H and He I lines (see Figs 9 and 10), which we attribute to the invasion of the OCSM by the shock. The broad lines persisted to at least day 1087 (Fassia et al., in preparation) with material still moving as fast as 4600 km s^{-1} relative to the SN centre of mass at that time. From this we infer that the OCSM extended at least as far as 1800 au from the supernova. For a wind velocity of 50 km s^{-1}, this implies that the ejection of the OCSM began at least 170 years ago, in agreement with L00. We agree with L00 that line ratios at this later time continue to imply a high density in the line-formation region of the OCSM. Our estimate for the deredenned [O III] ratio is

$(f_{\lambda 4959} + f_{\lambda 5007})/f_{\lambda 4363} = 2.5 \pm 0.9$ (average of values from days 72 and 97) which suggests (see Fig. 12) densities $n_e > 1.5 \times 10^6\,cm^{-3}$ for a temperature of $10^4 < T < 10^5$ K, consistent with the density derived at earlier epochs by us and by L00.

From the above we can obtain lower limits for the OCSM mass and for the mass-loss rate that produced it. Assuming that the OCSM has the form of a spherically symmetric wind of constant velocity v_w, the density would vary as $\propto r^{-2}$. Consequently, the mass of the OCSM is

$$M \gtrsim 4\pi r_{in}^3 m_H n \mu \left(\frac{r_{out}}{r_{in}} - 1\right), \quad (1)$$

where μ is the mean atomic weight in amu, m_H is the mass of the hydrogen atom, r_{in} and r_{out} are the inner and outer limits of the OCSM, and n is the total number density at the inner limit. Making the conservative assumption of complete ionization and that the OSCM consists mostly of hydrogen, we have $n \approx 2n_e$ and $\mu = 0.5$. Therefore, substituting $n_e \sim 1.5 \times 10^6\,cm^{-3}$, $r_{in} \sim 185$ au and $r_{out} \gtrsim 1800$ au, we have $M \gtrsim 0.003\,M_\odot$. For a wind velocity of $50\,km\,s^{-1}$ and a constant mass-loss, we obtain a mass-loss rate of $\gtrsim 2 \times 10^{-5}\,M_\odot\,yr^{-1}$ taking place for at least 170 years before the explosion.

4.2 Carbon monoxide

Molecular emission from a supernova was first observed in the form of CO emission from SN 1987A (Catchpole & Glass 1987; McGregor & Hyland 1987). Measurement of the first-overtone spectrum as early as day 110 was reported by Meikle et al. (1989). However, it is possible that CO formed even earlier. The sudden rise in the $K - M$ colour at about day 100 (Bouchet & Danziger 1993) may have been due to CO fundamental emission in the M band. The evolution of the SN 1987A first-overtone emission spectrum was monitored by Meikle et al. (1989, 1993) to 1.5 years. Other species responsible for molecular emission from SN 1987A include SiO, together with more tentative identifications of CS, FeO, H_3^+ and HeH^+ (Dalgarno, Stancil & Lepp 1997, and references therein). Of these molecules, emission from CO has been most extensively studied.

Analysis of the first-overtone CO band in SN 1987A has demonstrated the value of this type of study in determining the velocity, excitation temperature and CO mass in the CO-emitting zone. The first models (Spyromilio et al. 1988), which assumed LTE, provided good fits for days 192 and 255, implying a CO mass of $\sim 10^{-4}\,M_\odot$. Velocities of $2000\,km\,s^{-1}$ and $1800\,km\,s^{-1}$, respectively, were inferred for the two epochs. At later epochs poorer fits were obtained. This was attributed to deviation from a Boltzmann distribution. Subsequent interpretations by several groups involved non-LTE modelling for the vibrational transitions. An example is the work of Liu & Dalgarno (1995), who obtained much-improved fits for the late-time data. They inferred a mass of CO as high as $0.04\,M_\odot$ on day 110, but this was quickly reduced to $\sim 3 \times 10^{-3}\,M_\odot$ by day 250 due to destruction by the fast electrons. They found that, when present, the vibrational transitions of CO provide the dominant cooling mechanism of the C/O zone during the first two years, reducing the temperature to ~ 700 K by the end of that period. Prior to SN 1998S, the only other supernova (besides SN 1987A) for which CO emission has been detected is the type II SN 1995ad at around 105 days, observed by Spyromilio & Leibundgut (1996). Following Liu & Dalgarno, they suggest that a CO mass as high as $0.05\,M_\odot$ might have formed. In SN 1998S intense first-overtone CO emission spectra were measured at two epochs (days 110 and 240, with our definition of $t_0 =$ 1998 March 2.68 UT) by G00 and at a single epoch (day 109) by us. We shall compare their conclusions with ours at a later point in this section.

4.2.1 *Non-LTE model of CO emission*

To interpret the CO spectrum of SN 1998S, we have constructed a model by following a similar non-LTE approach to that of (Liu & Dalgarno 1995), including CO formation and gamma-ray energy deposition. The only additional feature is a simple treatment of non-local radiative coupling of the first-overtone lines in a clumpy envelope. By adjusting the model to reproduce our day 109 CO spectrum (Figs 8 and 13), we can estimate the mass, density, temperature and velocity of the CO and C/O-rich matter, as well as the mass of ^{56}Ni. To compare the model with the data, the model luminosity was converted to flux assuming a distance of 17 Mpc (Tully 1988).

In the model we assume that the CO emission arises from an ensemble of C/O-rich clumps embedded in a homogeneous (on average), macroscopically mixed core. All the C/O-rich clumps are composed of equal proportions by mass of C and O, and have similar size and physical conditions. Following Liu & Dalgarno (1995), we assume that the total mass of the clumped C/O-rich mixture is $M_{cl} = 0.2\,M_\odot$. This is reasonably consistent with mass estimates from stellar evolution computations for stars in the range $12–25\,M_\odot$ (Heger 1999). Gamma-ray energy deposition is determined using the escape probability approximation with an absorption coefficient of $k_\gamma = 0.03\,cm^2\,g^{-1}$. However, it is likely that the ^{56}Ni is also clumped. Consequently, as the gamma-rays travel from the ^{56}Ni clumps to the C/O-rich clumps they will suffer attenuation, the amount of which will decrease with age. This process has been invoked in SN 1987A to account for the slow evolution of the CO luminosity at early epochs (Liu & Dalgarno 1995). To allow for this effect in SN 1998S, we follow Liu & Dalgarno by including an energy reduction factor ψ by which the deposition rate in the C/O-rich material is multiplied. To estimate ψ for SN 1998S on day 109, we compared the first-overtone CO flux with that reported by G00 on day 225. The density of the C/O-rich clumps (ρ_{cl}) may be higher than the average density in the core (ρ_c), and so we specify the overdensity with a density contrast parameter $\chi = \rho_{cl}/\rho_c \geq 1$. The CO concentration is primarily controlled by CO formation via the radiative association $C + O \rightarrow CO + h\nu$, and destruction via ionization by fast electrons $CO + e \rightarrow CO^+ + e$ followed by the dissociative recombination $CO^+ + e \rightarrow C + O$ (Liu & Dalgarno 1995).

The fraction of deposited energy channelled into Coulomb heating was obtained using calculations of Kozma & Fransson (1992). The electron temperature (T_e) of the C/O-rich clumps was found assuming energy balance between the energy deposited as heat by Compton electrons and the radiation emitted in the CO fundamental and first-overtone bands. Cooling in [O I] 6300, 6364 Å lines was found to contribute typically less than 4 per cent of that due to the CO bands, in agreement with the analysis by Liu & Dalgarno (1995).

The non-LTE population of vibrational levels was calculated assuming that radiative and collisional transitions between neighbouring vibrational levels are dominant. This is a sensible approximation, since the radiative transition rates for the first

overtone are an order of magnitude smaller than those for the fundamental. The electron collision rate coefficients were taken from Liu, Dalgarno & Lepp (1992), while oscillator strengths are from Kirby-Docken & Liu (1978). 12 vibrational states, with 101 rotational levels for each vibrational state, were considered. This yields a line list of 2000 lines for the first-overtone band, and 2200 lines for the fundamental band. The CO radiative rates are affected by continuum radiation originating outside the clumps. The effects of this were determined by assuming that the core luminosity is equal to the overall deposited radioactive luminosity. The external continuum spectrum was approximated by a dilute blackbody with a colour temperature of 5000 K. In practice, the model is not very sensitive to the choice of the temperature, since the effect of the external continuum radiation is small compared to that of the collisions. This is in accordance with the Liu & Dalgarno (1995) conclusions about SN 1987A. After the populations of the vibrational levels were found, the rotational levels of individual vibrational states were populated according to the Boltzmann distribution.

Radiative transfer in the clumpy CO matter was treated in terms of the average escape probability. This includes the combined effects of the escape probability of photons from an average CO cloud, together with absorption by the other CO clouds in the core. Our models reveal that variation of the CO cloud radius between 10 and 100 km s^{-1} (assuming homologous expansion) only slightly affects the shape of the spectrum. We adopted a cloud radius of $a = 50\,\mathrm{km\,s^{-1}}$, very similar to the oxygen clump size estimates for SN 1987A (Stathakis et al. 1991). The weak sensitivity of the spectrum shape to the cloud size is due to the opposing trends of photon absorption in the CO emission source cloud and in other clouds.

The final model is specified using four free or 'input' parameters: core velocity (v_c), core mass (M_c), density contrast (χ), and ^{56}Ni mass (M_{Ni}). It should be stressed that not all these parameters are equally constrained by the observations. In particular, good fits over a wide core mass range may be achieved by simply adjusting the other three parameters appropriately. However, we find that models with a core mass $M_c < 0.4\,M_\odot$ require an implausibly high density contrast in the C/O-rich matter ($\chi \geq 10$). On the other hand, models with a core mass $M_c > 4\,M_\odot$ require a ^{56}Ni mass $>0.2\,M_\odot$, inconsistent with the bolometric luminosity of SN 1998S around day 130 (Fassia et al. 2000). We have therefore considered the two extreme cases set by these considerations, viz. model A with a core mass of $0.4\,M_\odot$, and model B with a core mass of $4\,M_\odot$.

4.2.2 *Comparison of the CO model with the day-109 spectrum.*

We find that both models are able to reproduce the observed CO first-overtone emission for plausible combinations of the free parameters v_c, χ and M_{Ni}. From these models we obtain physically reasonable values for the 'output' parameters M_{CO}, T_e, n_b (n_b is the density of the C/O-rich matter expressed as a baryon number density). In Fig. 13 we show model A fits for core velocities of 1600, 2200 and 2800 km s^{-1}. We can immediately eliminate the two extreme values. In the 1600 km s^{-1} model, the visibility of the quasi-periodic structure produced by the R-branches of the 0–2 and 1–2 vibrational transitions is too high. In the 2800 km s^{-1} model the visibility is too low, and the rising blue edge too shallow. We deduce that the velocity of the CO emission zone is $2200 \pm 300\,\mathrm{km\,s^{-1}}$. A similar result is obtained for model B. For

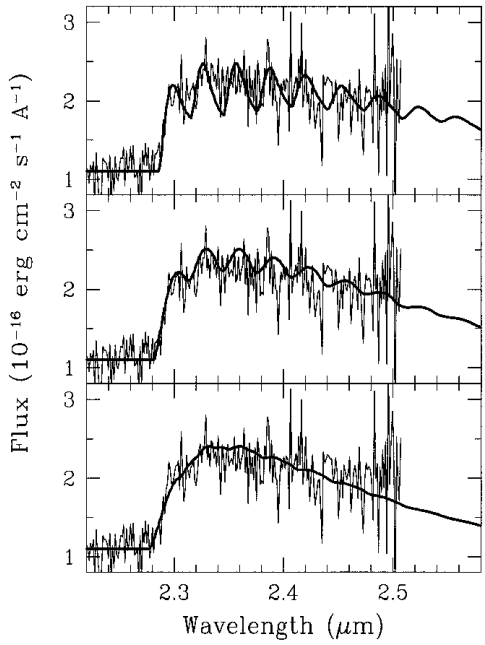

Figure 13. Carbon monoxide first-overtone model A (thick line) (cf. Table 6) compared with observations (thin line). Models are shown for three CO emission zone velocities: 1600 km s^{-1} (top panel), 2200 km s^{-1} (middle) and 2800 km s^{-1} (bottom).

Table 6. Carbon monoxide model parameters.

Model	Input parameters (see text)				Output parameters (see text)		
	M_c ($M_\odot$)	M_{Ni} ($M_\odot$)	χ	ψ	n_b (10^{11} cm^{-3})	M_{CO} ($10^{-3}\,M_\odot$)	T_e (K)
A	0.4	0.07	8	0.24	0.77	1.2	3700
B	4	0.2	1	0.52	0.97	1.3	3650

the optimum velocity of 2200 km s^{-1}, in Table 6 we show the input and output parameters for the two models.

We find that n_b, M_{CO} and T_e are quite similar for models A and B. To narrow down further the range of models encompassed by A and B, additional information is required. One such fact is the estimate by Fassia et al. (2000) of a ^{56}Ni mass of $0.15 \pm 0.05\,M_\odot$, based on the bolometric light curve of SN 1998S. This is consistent with model B but not model A (Table 6). A caveat is the possible contribution to the luminosity from the ejecta–wind interaction, which might decrease the ^{56}Ni mass implied by the bolometric light curve. However, Fassia et al. point out that the observed bolometric decline rate matches well the radioactive luminosity decay rate, arguing against a significant ejecta–wind contribution to the luminosity. Another argument in favour of model B is based on the issue of the energy reduction factor. The model A fit requires $\psi = 0.2$–0.3, indicating a substantial difference between the average intensity of gamma-rays in the ^{56}Ni zone and C/O-rich clumps. Yet, in this model the optical depth of the core for gamma-rays is only about 1. Moreover, macroscopic mixing should lead to even lower optical depths in the 'walls' between ^{56}Ni and C/O zones. These low optical depths are inconsistent with a ψ value as low as 0.2–0.3, as is required to fit the data. On the other hand, the version of model B rm which fits the observed spectrum has a core optical depth of $\sim$10 on day 109, consistent with its ψ value of $\sim$0.5 (Table 6).

In summary, we favour the high mass core model (model B)

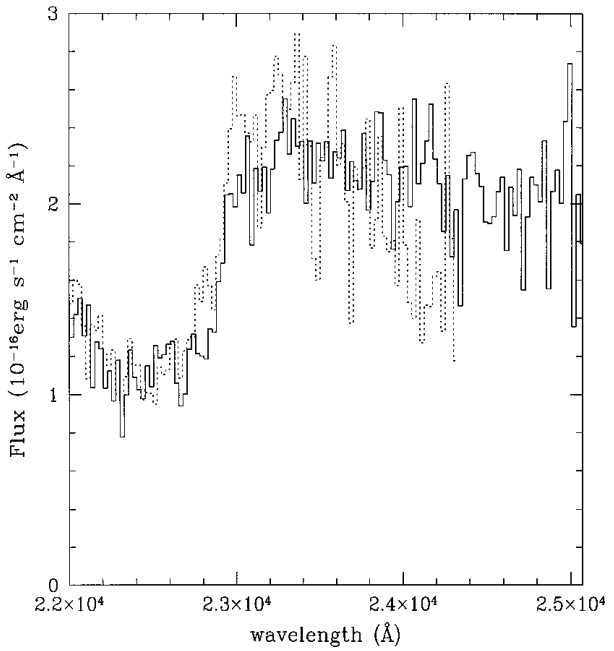

Figure 14. Comparison of the first-overtone CO spectrum obtained on day 109 (solid line) with the spectrum obtained by G00 on day 110 (dotted line). The spectra have not been corrected for the redshift of the supernova.

with a core mass of $4\,M_\odot$, core velocity of $2200 \pm 300\,km\,s^{-1}$, electron temperature of 3650 ± 200 K, negligible overdensity of the C/O-rich clumps (density contrast parameter $\chi \sim 1$), and a ^{56}Ni mass of about $0.2\,M_\odot$. (Note that the C/O is still clumped in the sense of chemical abundance.) Unfortunately, the mass of the mixed core does not permit us to draw definite conclusions about the progenitor mass. The reason is that we lack information about the relative proportions of metal-rich and H/He-rich materials in the core. That the amount of H/He-rich material might be significant is supported by the observation of sharp-topped Hα and He I 10 830-Å line profiles at $t \approx 100$ d, indicating the presence of low-velocity hydrogen and helium ($v \approx 1000\,km\,s^{-1}$).

G00 have analysed the CO emission from SN 1998S covering about the same epoch as did our study. Matching their day 110 CO first-overtone spectrum with a range of models, they deduce a CO velocity of 2000–3000 $km\,s^{-1}$. They argue that a CO velocity of $3000\,km\,s^{-1}$ would imply a progenitor mass in excess of $25\,M_\odot$, which is outside the plausible progenitor mass range for our adopted C/O-rich core mass. However, we believe that our analysis eliminates the upper half of their velocity range, which presumably would reduce the inferred progenitor mass. Yet in any event, as pointed out above, there are difficulties in reaching firm conclusions about the progenitor mass. We note that G00's CO velocity value depends quite strongly on the presence in their spectrum of a 'smooth rise to the blue edge of the CO feature'. However, our spectrum, taken within a day of theirs, does not show this smooth rise. Instead, our spectrum remains roughly flat to about 2.27 μm, and then rises abruptly. In Fig. 14 we compare the two spectra, binned to 25 Å per pixel. It can be seen that the agreement is excellent up to 2.27 μm, but then the spectra become more discrepant. In particular, the G00 spectrum exhibits a 'bump' at about 2.28 μm, which contributes significantly to the perception of their smooth rise to the blue edge. However, their spectrum appears to be rather noisy redward of 2.3 μm, and it may be that noise is also responsible for their 2.28-μm bump. Our value for the electron temperature, 3450–3850 K, also confines the 3000–4000 K range suggested by G00.

As indicated above, Liu & Dalgarno (1995) deduce a CO mass of $\sim 10^{-2}\,M_\odot$ in SN 1987A at 110 d, which is an order of magnitude greater than for SN 1998S at a similar epoch (cf. Table 1). The reason for this is that the ^{56}Ni mass and the energy reduction factor, ψ, are both 3 times lower for SN 1987A than for SN 1998S, leading to ~10 times more efficient CO formation in SN 1987A.

5 CONCLUSIONS

We have presented and discussed optical and infrared spectra of the type IIn SN 1998S, covering epochs from a few days after explosion to over 100 days later. Our observational coverage of SN 1998S makes a significant contribution to the study of the type IIn phenomenon. Of particular note is our acquisition of (a) contemporary spectra in both the optical and IR bands at a range of epochs, and (b) the most extensive set of high-resolution spectra ever for this type of supernova event. The spectroscopic evolution of SN 1998S was complex. It can be understood in terms of the interaction of the supernova with a two-component progenitor wind, which we have referred to as the ICSM and OCSM.

Collision of the ejecta with the ICSM accounts for the early spectral features. From the fading of the broad emission components by about day ~14 we deduce that the outer boundary of this wind lay at less than 90 au from the centre. Estimation of the inner wind velocity is difficult due to (a) the ongoing interaction of the shock with this wind even at the earliest of times, and (b) the lack of high-resolution spectra at these times. We can only say that the early-time spectra exhibited features of width less than $400\,km\,s^{-1}$. However, these may have arisen in the OCSM. If, like L00, we assume that the inner and outer winds had similar velocities, then from our high-resolution measurements of the OCSM we can infer that the ICSM wind commenced less than 9 years ago. However, the possibility of an RSG–BSG evolution would argue against this assumption.

Examination of the spectra indicates that the OCSM extended from 185 au to over 1800 au. Our high-resolution spectra have revealed that the OCSM has a velocity of 40–50 $km\,s^{-1}$. Assuming a constant velocity during this time, we can infer that it commenced more than 170 years ago, and ceased about 20 years ago. During this period the outflow was high – at least $2 \times 10^{-5}\,M_\odot\,yr^{-1}$, corresponding to a mass-loss of at least $0.003\,M_\odot$. An outflow of this strength and velocity is similar to those seen in cool supergiants. The broader absorption feature ($\sim 350\,km\,s^{-1}$) in H and He I may have arisen from a component of the outer CSM shell produced when the progenitor was going through a later blue supergiant phase. Alternatively, it may have been due to UV-precursor radiative acceleration of the inner part of the OCSM.

Our analysis of the CO emission, together with the bolometric light curve (Fassia et al. 2000), also indicates a massive progenitor, with a mixed metal/He core of $M \sim 4\,M_\odot$, i.e., comparable to that of SN 1987A. SN 1998S is only the third core-collapse SN for which post-day 100 *K*-band spectra have been published, and yet all SN three events have exhibited first-overtone CO emission. (Fassia et al. (1998) also published IR spectra for the core-collapse SN 1995V. No CO was identified, but the latest *K*-band spectrum was only at day 69.) A picture is therefore beginning to emerge where CO plays a ubiquitous role in the evolution of core-collapse SNe at late times. In particular, the

powerful cooling property of CO is likely to lead to conditions in which dust may condense in the ejecta. Excess IR emission has been reported in SN 1998S on days 225, 260 and 255 (G00), day 253 (Garnavich, Jha & Kirshner 1998), and for a series of dates to as late as day 1043 (Fassia et al. in preparation), and this may be due to dust condensation. (An IR excess at day 130 was also reported by Fassia et al. 2000, but they argue that it was unlikely to have arisen from dust condensation.) In a future paper (Fassia et al., in preparation) we shall examine in detail the evolution of the late-time IR excess.

L00 used spectropolarimetry at early times to infer significant asymmetry in the OCSM and in the ejecta–ICSM interface. While our discussion of the high-resolution OCSM lines assumed spherical symmetry, we have not provided quantitative explanations for the relative shifts between the allowed and forbidden lines. It may be that this will also require the introduction of an asymmetric model. G00 also deduced asymmetry in the OCSM, on the basis of the broad line profiles of H and He on days 240, 275 and 370. We shall discuss these profiles in a future paper.

ACKNOWLEDGMENTS

We thank Janet Drew and Leon Lucy for helpful discussions. We also thank Daryl Willmarth for obtaining some of the WIYN data. The WIYN Observatory is a joint facility of the University of Wisconsin-Madison, Indiana University, Yale University, and the National Optical Astronomy Observatories. The INT and WHT are operated on the island of La Palma by the Isaac Newton Group in the Spanish Observatorio del Roque de los Muchachos of the Instituto de Astrofisica de Canarias. We also acknowledge that some of the data presented here were obtained as part of the UKIRT Service Programme.

REFERENCES

Abbott D. C., Bieging J. H., Churchwell E., 1981, ApJ, 250, 645
Aggarwal K. M., 1993, ApJS, 85, 197
Bessel M. S., 1979, PASP, 91, 589
Blanton E. L., Schmidt B. P., Kirshner R. P., Ford C. H., Chromey F. R., Herbst W., 1995, AJ, 110, 2868
Bowen D. V., Roth K. C., Meyer D. M., Blades J. C., 2000, ApJ 536, 225
Branch D., Jeffery D. J., Blaylock M., Hatano K., 2000, PASP, 112, 217
Broeils A. H., van Woerden H., 1994, A&AS, 107, 129
Bouchet P., Danziger I. J., 1993, A&A, 273, 451
Bowen D. V., Roth K. C., Meyer D. M., Blades J. C., 2000, ApJ, 536, 225
Cardelli J., Clayton G., Mathis J., 1989, ApJ, 345, 245
Catchpole R. M., Glass I. S., 1987, IAU Circ. 4457
Chevalier R. A., Fransson C., 1994, ApJ, 420, 268
Chugai N. N., 1990, SvA Lett., 16, 457
Chugai N. N., Danziger I. J., 1994, MNRAS, 268, 173
Cumming R. J., Meikle W. P. S., Walton N. A., Lundqvist P., 1994, in Clegg R. E. S., Meikle W. P. S., Stevens I. R., eds, Circumstellar Media in Late Stages of Stellar Evolution. Cambridge Univ. Press, Cambridge, p. 792
Dalgarno A., Stancil P. C., Lepp S., 1997, Ap&SS, 251, 375
Daly P. N., Beard S. M., 1992, Starlink User Note 27.1,
de Vaucouleurs G., de Vaucouleurs A., Corwin, Jr., Buta R. J., Paturel G., Fouqué P., 1991, Third Reference Catalogue of Bright Galaxies, version 3.9
Dupree A. K., 1986, ARA&A, 24, 377
Fassia et al., 2000, MNRAS, 318, 1093
Fassia A., Meikle W. P. S., Geballe T. R., Walton N. A., Pollacco D. L., Rutten R. G. M., Tinney C., 1998, MNRAS, 299, 150
Filippenko A. V., Moran E. C., 1998, IAU Circ. 6830,
Fouqué P., Durand N., Bottinelli L., Gouguenheim L., Paturel G., 1992, Catalogue of Optical Radial Velocities, Vol. 1
Fransson C., Lundqvist P., Chevalier R. A., 1996, ApJ, 461, 993
Galavis M. E., Mendoza C., Zeippen C. J., 1997, A&AS, 123, 159
Garnavich P., Jha S., Kirshner R., 1998, IAU Circ. 6832
Garnavich P., Jha S., Kirshner R., Gerardy C., Fesen R., Calkins M., Szentgyorgyi A., 1998, IAU Circ. 7058
Garnavich P. et al., 1999, http://cfa-www.harvard.edu/cfa/oir/Research/supernova/spectra/sn98s_lightcurve.gif
Gerardy C. L., Fesen R. A., Höflich P., Wheeler J. C., 2000, AJ, 119, 2968 [G00]
Heger A., 1999, PhD dissertation, MPA 1120. Max-Planck Institute für Astrophysik, Garching
Ho L. C., Filippenko A. V., Sargent W. L., 1995, ApJS, 98, 477
Horne K., 1986, PASP, 98, 609
Jura M., Kleinmann S. G., 1990, ApJS, 73, 764
Kirby-Docken K., Liu B., 1978, ApJS, 36, 359
Kozma C., Fransson C., 1992, ApJ, 390, 602
Lentz E. J. et al., 2001, ApJ, 547, 406
Leonard D. C., Filippenko A. V., Barth A. J., Matheson T., 2000, ApJ, 536, 239 [L00]
Li W. D., Wan Z., 1998, IAU Circ. 6829,
Liu W., Dalgarno A., 1995, ApJ, 454, 472
Liu W., Dalgarno A., Lepp S., 1992, ApJ, 396, 679
Lundqvist P., Fransson C., 1988, A&A, 192, 221
Maran P. S., Sonneborn G., Pun C. S. J., Lundqvist P., Iping R. C., Gull T. R., 2000, ApJ, 545, 390
McGregor P., Hyland A. R., 1987, IAU Circ. 4468
Meikle W. P. S., Allen D. A., Spyromilio J., Varani G-F., 1989, MNRAS, 238, 193
Meikle W. P. S., Spyromilio J., Allen D. A., Varani G.-F., Cumming R. J., 1993, MNRAS, 261, 535
Osterbrock D. E., Fulbright J. P., Martel A., Keane M. J., Trager S. C., 1996, PASP, 108, 277
Press W. H., Teukolsky S. A., Vettering W. T., Flannery B. P., 1992, Numerical Recipes, 2nd ed. Cambridge Univ. Press, Cambridge
Qiu Y. L., Yoshida S., Merlin J. C., Schmeer P., 1998, IAU Circ. 6835
Salasnich B., Bressan A., Chiosi C., 1999, A&A., 342, 131
Schlegel E. M., 1990, MNRAS, 244, 269
Shortridge K., 1995, FIGARO General Data Reduction and Analysis Starlink MUD, RAL, June 1991
Spyromilio J., Leibundgut B., 1996, MNRAS, 283, 89
Spyromilio J., Meikle W. P. S., Learner R. C. M., Allen D. A., 1988, Nat, 334, 327
Stathakis R. A., Dopita M. A., Cannon R. D., Sadler E. M., 1991, in Woosley S. E., eds, Supernovae. The Tenth Santa Cruz Workshop in Astronomy and Astrophysics. Springer-Verlag, New York, p. 95
Terlevich R., Tenorio-Tagle G., Franco J., Melnick J., 1992, MNRAS, 255, 713
Tully R. B., 1988, Nearby Galaxies Catalog. Cambridge Univ. Press, Cambridge
Williams R. E., 1987, ApJ, 320, L117
Wilson W. J., Schwartz P. R., Neugebauer G., Harvey P. M., Becklin E. E., 1972, ApJ, 177, 523

This paper has been typeset from a TEX/LATEX file prepared by the author.